Neural mechanisms of training in Brain-Computer Interface : A Biophysical modeling approach

Apurba Debnath[1] Tristan Venot[2] Marie-Constance Corsi[2,*] Parul Verma[1,3,*]

[1]Centre for Integrative Biology and Systems Medicine, Indian Institute of Technology Madras, Chennai, India
[2]Sorbonne Université, Institut du Cerveau—Paris Brain Institute—ICM, CNRS, Inria, Inserm, AP-HP, Hôpital de la Pitié Salpêtrière, F-75013 Paris, France
[3]Department of Chemical Engineering, Indian Institute of Technology Madras, Chennai, India
[*]Corresponding authors. Email: marie-constance.corsi@inria.fr, parulv@iitm.ac.in

Abstract

Brain-Computer Interface (BCI) is a system that translates neural activity into commands, allowing direct communication between the brain and external devices. Despite its clinical application, BCI systems are unable to robustly capture subjects' intent due to a limited understanding of the neural mechanisms underlying BCI control. To address this issue, we introduce a biophysical linear neural mass model to investigate the associated neural mechanisms of motor imagery-based BCI experiments by modulating the scale-free spectral characteristics of afferent inputs. We tailor this motor imagery neural mass model (mi-NMM) to simulate both motor imagery task and resting state, and apply this approach to a cohort of 19 healthy subjects trained over four sessions where magnetoencephalography (MEG) and electroencephalography (EEG) signals were simultaneously recorded. Task-dependent modulation of scale-free cortical dynamics reveals training-induced excitatory–inhibitory reconfiguration in BCI training. The intra-regional neural connectivity strengths and time scales of the modeled excitatory and inhibitory neural mass populations capture changes in neural activity across conditions and sessions. Those changes appear in important areas of the sensorimotor cortex, relevant for motor imagery tasks. We observed these effects in both EEG and MEG modalities. These findings provide insights into the underlying neural mechanisms in a motor imagery task in BCI, paving the way to tailored BCI training protocols.

Keywords: Brain-computer interface, Neural mass model, EEG, MEG, Motor imagery, Biophysical model

Significance Statement

Brain–computer interface (BCI) holds great promise in allowing direct communication between the brain and external devices, yet many users struggle to learn it reliably, largely because the neural mechanisms underlying BCI training remain poorly understood – thus lack of biologically grounded training protocols. This study introduces a biophysically grounded modeling framework that links large-scale brain dynamics to learning during motor imagery based BCI training. By explicitly modeling task-dependent cortical background input, we reveal how excitatory–inhibitory population dynamics reorganize with training, shifting from widespread cortical to targeted sensorimotor recruitment. Our results, replicated across EEG and MEG, identify excitatory population time scales as a robust neural marker of motor imagery learning. These findings provide mechanistic insight into BCI learning and offer principled targets for designing individualized BCI training protocols.

1 Introduction

Brain-Computer Interfaces (BCIs) enable the brain to directly control external devices by translating neural activity into actionable commands, but developing a control system based on brain signals is a formidable challenge. BCIs necessitate the acquisition of intricate neural data and the conversion of these signals into dependable commands, all within the constraints of an incomplete understanding of brain function (1; 2). Despite these obstacles, BCIs hold significant promise, particularly in clinical applications, where they enable direct brain-to-device communication to compensate for lost motor or sensory functions (3).

Nonetheless, non-invasive methods such as electroencephalography (EEG) and magnetoencephalography (MEG) often provide limited control for many users (4). While training can enhance BCI performance, a critical question persists: why do some users exhibit substantial improvement while others face ongoing difficulties? This issue is particularly evident in motor imagery-based BCIs (MI-BCI), where users operate a device by imagining movements without physically executing them. Numerous studies have attempted to address the various ambiguities in this field, including enhancing brain signal decoders (5), identifying neurophysiological and psychological factors affecting user performance (6; 7; 8), and developing improved training protocols (9). A critical element believed to be essential for successful BCI control is neuroplasticity, which underlies the brain's capacity to adapt and learn. This has spurred increasing interest in the neurophysiological mechanisms involved in neurofeedback and BCI learning (10). Furthermore, the phenomenon of BCI inefficiency has been examined from multiple perspectives. Learning to use a BCI differs fundamentally from interacting with intuitive, everyday tools; it requires mastering a new, abstract form of control. It is reasonable to infer that specific brain mechanisms are involved when a user learns to perform effectively in a BCI task.

Learning is increasingly understood not merely as a localized change in neural activity, but as a reconfiguration of the brain's overall dynamic state (11). A key signature of this state is the scale-free structure of brain signals, reflected in power-law relationship across frequencies, which is thought to arise from coordinated synaptic inputs. Importantly, this scale-free activity is not static; rather, it changes dynamically with task demands and cognitive states (12; 13). However, it remains unclear how these task-driven shifts contribute to the reorganization of excitatory-inhibitory (E/I) interactions during learning, underscoring the need for biophysical models capable of elucidating the brain processes involved in BCI learning and adaptation.

A class of biophysical models that have been particularly useful for these purposes is called the "Neural Mass Models" (NMMs) (14). NMMs model the population-level activity of interactions between excitatory and inhibitory neurons in different brain regions that potentially underlies the macroscopic signals we observe with E/MEG. As a result, they provide biophysical insights into how macroscopic signals may arise in various neurological conditions/diseases. Although these models have been used widely, they have rarely been investigated in the case of BCI, potentially because of the additional challenge of modeling the tasks appropriately. Indeed, most modeling studies focus on the resting state (RS) with limited attempts to model BCI-related tasks (15; 16). In this study, we developed a novel approach to model MI-BCI, called mi-NMM, that explicitly accounts for the brain's scale-free dynamics, capturing the prevalent arrhythmic activity that co-exists, yet is distinct from, brain oscillations. It leverages a linearized NMM that accurately captures the spectral features of the neural oscillatory activity estimated from source-localized MEG in healthy individuals in the RS (17; 18). This NMM has also been successful in identifying cortical-level neural impairments in patients with Alzheimer's disease (19) as well as neural modulations in healthy individuals transitioning from wakefulness to light sleep (20).

Using this approach, we hypothesized that key spectral differences between MI and RS result from region-specific, population-level interactions between excitatory and inhibitory neural subpopulations. Furthermore,

we posited that such region-specific changes could capture the neural mechanisms occurring during learning. To validate these hypotheses, we utilized source-reconstructed EEG and MEG signals obtained during a four-session MI-BCI training from healthy subjects.

2 Materials & Methods

2.1 Brain-Computer Interface data collection and analysis

In this study, we worked with a dataset composed of a cohort of 19 healthy right-handed subjects (mean age:27.4 ± 4.0 years; 12 men) participated in a BCI study. All participants were BCI-naive, free from medical or psychological disorders, and provided their written informed consent in accordance with the Declaration of Helsinki. The study was approved by the ethical committee CPP-IDF-VI of Paris.

Subjects underwent a two-week motor imagery-based BCI training program consisting of four sessions. At the beginning of each session, the subjects underwent a 3-minute RS with eyes opened. The BCI experiments consisted of a standard one-dimensional, two-target box task (21), where subjects controlled the vertical position of a cursor moving at a constant velocity from left to right to reach a target displayed on the right part of the screen. To reach the up target, the subjects were instructed to perform sustained right-hand motor imagery (MI) by modulating neural activity in the alpha (8–12 Hz) and beta (13–30 Hz) frequency bands. To hit the down target, the subjects had to remain at rest–which we refer here as baseline condition. Each of the six runs consisted of 32 trials, distributed equally and randomly among the targets.

Neural activity was recorded using simultaneous EEG and MEG modalities with a 74-channel EEG system (Ag/AgCl passive sensors, Easycap, Germany) following the 10-10 montage. MEG data were acquired using 102 magnetometers and 204 gradiometers (Elekta Neuromag TRIUX) in a magnetically shielded environment. The signals were sampled at 1 kHz (0.01–300 Hz bandwidth) and then downsampled to 250 Hz. MEG signals were preprocessed with temporal Signal Space Separation using MaxFilter (22). Eye and cardiac artifacts were removed from EEG/MEG signals via Independent Component Analysis with the Infomax approach in FieldTrip (23; 24). EEG electrodes T9 and T10 were excluded from further analysis. Source reconstruction was performed using the Boundary Element Method (25; 26) with three-layer MRI-derived surfaces (scalp, inner skull, outer skull; 1922 vertices each). The weighted Minimum Norm Estimate (27; 28; 29) was used to estimate cortical sources via Brainstorm (30), with an identity noise covariance matrix. The dipole orientations were constrained to the cortex. Individual source estimates were projected onto the MNI-ICBM152 template (31) using Shepard's interpolation.

Power spectra were calculated for each subject, session, and condition in the source space using the Welch method (1 s window, 50% overlap). For the rest condition, the estimation was performed directly from the 3-minute recording. For the MI condition, the power spectra were computed from the feedback period (t = 3–6 s) and averaged across trials. To localize the anatomical structures associated with the obtained clusters, we used the Desikan killiany (DK) atlas (32) without restricting the analysis to the motor or sensorimotor regions. The dataset was structured as (19 × 68 × 126) per session and condition, where 19 represents subjects, 68 corresponds to DK atlas-defined brain regions, and 126 represents frequency bins used in spectral analysis.

For more information on the experiment and the data processing, please refer to (33).

2.2 Model description

We used a linearized NMM (17; 18; 19) to extract excitatory and inhibitory neuronal subpopulation parameters. The model at the mesoscopic level (regional model), for every region k (k varies from 1 to N and N is the total number of regions) based on the DK parcellation, is modeled as the sum of excitatory signals

$x_{\mathrm{e}}(t)$ and inhibitory signals $x_{\mathrm{i}}(t)$. Both excitatory and inhibitory signal dynamics consist of a decay of the individual signals with a fixed neural gain, incoming signals from populations that couple the excitatory and inhibitory signals, and input Gaussian white noise for resting state and colored noise for mentally active state. The model equations for the excitatory and inhibitory signals for every region of the DK atlas that describes the rate of change of signal or firing rate in excitatory and inhibitory neural sub-populations are:

$$\frac{\mathrm{d}x_{\mathrm{e}}(t)}{\mathrm{d}t} = -f_{\mathrm{e}}(t) \star \frac{1}{\tau_{\mathrm{e}}}\big(g_{\mathrm{ee}}x_{\mathrm{e}}(t) - g_{\mathrm{ei}}f_{\mathrm{i}}(t) \star x_{\mathrm{i}}(t)\big) + p(t) \text{ , and} \tag{1}$$

$$\frac{\mathrm{d}x_{\mathrm{i}}(t)}{\mathrm{d}t} = -f_{\mathrm{i}}(t) \star \frac{1}{\tau_{\mathrm{i}}}\big(g_{\mathrm{ii}}x_{\mathrm{i}}(t) + g_{\mathrm{ei}}f_{\mathrm{e}}(t) \star x_{\mathrm{e}}(t)\big) + p(t) \text{ .} \tag{2}$$

The symbols used in the equations are as follows: $\star$ denotes convolution; parameters g_{ee}, g_{ii}, and g_{ei} represent neural gains for excitatory, inhibitory and for coupling neural gain between excitatory and inhibitory populations, respectively; τ_{e} and τ_{i} are the time scales of excitatory and inhibitory populations, respectively; $p(t)$ is extrinsic presynaptic input/stimulus; $f_{\mathrm{e}}(t)$ and $f_{\mathrm{i}}(t)$ are average neural impulse response functions. Parameters g_{ei}, g_{ii}, τ_{e}, and τ_{i} were estimated for each region of interest (ROI), while g_{ee} was fixed at 1 for parameter identifiability. The excitatory and inhibitory time scales characterize the duration of neural responses (modeled by a gamma-shaped function) in each neuronal subpopulation. They also determine the rate at which a local signal dissipates in the absence of other inputs. A lower time scale indicates a faster rate of change in signals, whereas a higher time scale corresponds to a slower rate. The neural gain parameters: excitatory (g_{ee}) and inhibitory (g_{ii}) neural gain represent the strength of self-excitatory and self-inhibitory feedback gain within their respective neuronal subpopulations, and the coupling excitatory-inhibitory (E/I) neural gain (g_{ei}) reflects the strength of interaction between the two subpopulations, as in how one subpopulation influences the activity of the other.

We can get a closed-form solution in the Fourier domain since the two equations above are linear, as shown below. The Fourier transform $F()$ is taken at an angular frequency ω, which is equal to $2\pi f$, where f is the frequency in Hz. The Fourier transform of equations 7 and 8 will be the following, where $F(x_{\mathrm{e}}(t)) = X_{\mathrm{e}}(\omega)$ and $F(x_{\mathrm{i}}(t)) = X_{\mathrm{i}}(\omega)$, and j is the imaginary unit.

$$\mathrm{j}\omega X_{\mathrm{e}}(\omega) = -\frac{F_{\mathrm{e}}(\omega)}{\tau_{\mathrm{e}}}(g_{\mathrm{ee}}X_{\mathrm{e}}(\omega) - g_{\mathrm{ei}}F_{\mathrm{i}}(\omega)X_{\mathrm{i}}(\omega)) + P(\omega) \text{ , and} \tag{3}$$

$$\mathrm{j}\omega X_{\mathrm{i}}(\omega) = -\frac{F_{\mathrm{i}}(\omega)}{\tau_{\mathrm{i}}}(g_{\mathrm{ii}}X_{\mathrm{i}}(\omega) + g_{\mathrm{ei}}F_{\mathrm{e}}(\omega)X_{\mathrm{e}}(\omega)) + P(\omega) \text{ .} \tag{4}$$

On solving the above equations 9 and 10, $X_{\mathrm{e}}(\omega)$ and $X_{\mathrm{i}}(\omega)$ are:

$$X_{\mathrm{e}}(\omega) = \frac{1 + \frac{F_1}{\tau_{\mathrm{e}}F_2}}{F_3 + \frac{F_1^2}{\tau_{\mathrm{e}}\tau_{\mathrm{i}}F_2}}P(\omega) \text{ , and}$$

$$X_{\mathrm{i}}(\omega) = \frac{1 - \frac{F_1}{\tau_{\mathrm{i}}F_3}}{F_2 + \frac{F_1^2}{\tau_{\mathrm{e}}\tau_{\mathrm{i}}F_3}}P(\omega) \text{ ,}$$

where

$$F_1 = g_{\mathrm{ei}}F_{\mathrm{e}}(\omega)F_{\mathrm{i}}(\omega), \quad F_2 = \mathrm{j}\omega + \frac{g_{\mathrm{ii}}}{\tau_{\mathrm{i}}}F_{\mathrm{i}}(\omega), \quad \text{and} \quad F_3 = \mathrm{j}\omega + \frac{g_{\mathrm{ee}}}{\tau_{\mathrm{e}}}F_{\mathrm{e}}(\omega).$$

Then, the transfer functions $H_{\mathrm{e}}(\omega)$ and $H_{\mathrm{i}}(\omega)$ can be separated, and we get:

$$X_{\mathrm{e}}(\omega) = H_{\mathrm{e}}(\omega)P(\omega), \quad \text{and} \quad X_{\mathrm{i}}(\omega) = H_{\mathrm{i}}(\omega)P(\omega).$$

Thus, for the total neural population at each region:

$$X_{\text{local}}(\omega) = (H_{\mathrm{e}}(\omega) + H_{\mathrm{i}}(\omega))P(\omega) \tag{5}$$

The extrinsic input $p(t)$ is characterized by its power spectral density (PSD) $S_p(\omega)$, which is assumed to be identical for excitatory and inhibitory local populations within each region. To simulate RS condition, $p(t)$ was modeled as white noise, characterized by a constant PSD. To simulate the MI condition, $p(t)$ was modeled as a colored noise with a power-law spectrum, such that $S_p(\omega) \propto 1/f^k$, where $k \in [0, 1]$.

Given the linear time-invariant nature of the model, the simulated output power spectral density was obtained as:

$$S_{X_{\text{local}}}(\omega) = \mathbb{E}[|X_{\text{local}}(\omega)|^2] \propto |(H_{\mathrm{e}}(\omega) + H_{\mathrm{i}}(\omega))|^2 S_p(\omega) \tag{6}$$

where $\mathbb{E}[\cdot]$ denotes expectation. The resulting spectra were expressed in dB scale as $10 \log_{10} S_{X_{\text{local}}}(\omega)$. Thus, overall in the end we are only interested in the PSD of the signal. See the supplementary document for more details.

2.3 Model parameter estimation

Model parameters were estimated for each region, each subject, and across all sessions, for frequency range of [3-30] Hz. For every subject, each region's spectrum was modeled using equations 9 and 10, and finally the total spectrum obtained from equation 11 was compared to the empirical spectrum. The goodness of fit of the model was evaluated by calculating Pearson's correlation coefficient (r) between the modeled power spectra and the empirical source-localized (E/MEG) spectra. This goodness-of-fit value was used to optimize the model parameters.

All the model parameters were set within a biophysically realistic range based on prior experiments (17), and the parameter optimization was performed using the basin-hopping global optimization algorithm in Python (34). The initial guess for all parameters and the parameter bounds used for estimating the modeled spectra are provided in Table 1. To ensure model stability, we defined five different bounds for the coupling excitatory-inhibitory neural gain (g_{ei}) (35). Initially, a larger bound was applied to g_{ei}, and if the optimal model parameter crossed the stability boundary, the optimization was repeated with a smaller bound. This process was iterated up to five times to ensure that the final optimal parameters corresponded to stable model solutions. The model parameters and their bounds are specified in Table 1. In addition to these parameters, the color of the input noise was also optimized for in the case of MI, within the range of [0,1] as mentioned in the previous section. Importantly, all the intrinsic model parameters (g_{ei}, g_{ii}, τ_{e}, τ_{i}) were estimated independently for each subject, region, session, and condition, and were allowed to vary freely within their respective bounds during optimization to maximize the goodness of fit between modeled and empirical spectra.

The algorithm's hyperparameters included the number of iterations (`niter`), temperature (`T`), and step size (`stepsize`), which were set to 5000, 0.1, and 4, respectively. If any parameter hit the specified bounds, the optimization was repeated with a step size of 6 for that specific ROI. Finally, the set of parameters yielding the highest Pearson's correlation coefficient was selected. The cost function for optimization was defined as the negative Pearson's correlation coefficient between the source-localized (E/MEG) spectra in the dB scale and the model power spectral density in the dB scale.

Table 1: Model parameters with biophysically realistic initial guesses, and bounds for estimating the spectra

Parameters	**Symbol**	**Initial guess**	**Lower/upper bound for optimization**
Excitatory time scale (ms)	τ_{e}	17	[5.0, 30.0] (Same in all 5 bounds)
Inhibitory time scale (ms)	τ_{i}	17	[5.0, 30.0] (Same in all 5 bounds)
Excitatory-Inhibitory neural gain	g_{ei}	0.4	[0.001, 0.7], [0.001, 0.5], [0.001, 0.4], [0.001, 0.3], [0.001, 0.25]
Inhibitory neural gain	g_{ii}	1.0	[0.001, 1.9] (Same in all 5 bounds)

As this is the first pilot study, we started with comparing the most contrasting conditions. Therefore, we focused on the resting state recorded before the BCI experiment was started, and the MI performed during the BCI training. Specifically, we did not include the baseline condition in which subjects were instructed to remain at rest during the BCI training – the baseline condition may not correspond to strictly being in the resting state as the subjects can still continue to think about the experiment/their performance. A workflow of this modeling approach is shown in Fig. 1.

2.4 Statistical analyses

To examine the potential condition effect as in, significant difference between motor imagery (MI) and resting state (RS) in each session separately, we performed Wilcoxon signed rank test (36) on all four intrinsic model parameters across 19 subjects. We chose this non-parametric Wilcoxon test as the model derived biophysical parameters were not normally distributed. This analysis was conducted for each ROI to compare MI and RS conditions for all four parameters. For each session, we obtained 68 p-values (one for each brain region based on the DK atlas) per parameter, thus four sets of 68 p-values per session (one set for each parameter). Thereafter, we applied the false discovery rate (FDR) correction (37) to each of the four sets to account for multiple comparisons. We set a significance threshold at $p_{\mathrm{FDR}} < 0.05$ to identify statistically significant regions for these parameters individually. The brain regions that met this significance criterion were identified for each parameter separately in each session. We used the same procedure both for EEG and MEG.

Next, we analyzed how the session affected MI and RS in both M/EEG. We used the Friedman test (38) on the statistically significant left motor regions for the corresponding parameter from the session 4 condition effect analysis. Then, we corrected the two p-values (as two regions in left motor area in MEG) using the Bonferroni correction method. Thereafter, we examined session-wise relationship between excitatory time constant (τ_{e}) and group-level BCI performance using linear mixed-effects models (LMM) (39). Here, the BCI score is set as dependent variable, regional excitatory time constant (τ_{e}) as a fixed effect, session as a fixed categorical factor, and subject as a random intercept to account for repeated measurements within subjects across sessions (Model: Score $\sim \tau_{\mathrm{e}}$ + Session + (1 | Subject)). LMM models were fitted independently for each of the 68 regions, and FDR correction was applied across regions. Furthermore, to relate the model parameters to event-related desynchronization (ERD) and synchronization (ERS) dynamics, we conducted Spearman's rank correlation test between ERD/S and relative parameter (MI/RS-1) across all 68 regions for each session. Repeated measure correlation was performed to assess within subject coupling between $\Delta\tau_{\mathrm{e}}$ and ERD/S across sessions, accounting for the non-independence of repeated measurements across sessions. Analyses were performed for each of the 68 regions, and the resulting p values were corrected for multiple comparisons using FDR correction.

3 Results

3.1 Simulating modeled input as colored noise better captures MI power spectra in M/EEG

The NMM for the excitatory/inhibitory neural population signals incorporates decay of these signals over time, interactions among them, and an external input. We assume that this external input/stimulus refers to background neural activity under resting state (RS) condition, arising as aggregate extrinsic presynaptic input, which is considered to be largely asynchronous and weakly correlated. Accordingly, following previous studies (17; 19; 18; 40; 41; 42; 15) we model this input $p(t)$ as white noise in Equation (12), characterized by constant power spectral density, for all region of interests (ROIs), sessions and subjects. In contrast, during active task engagement such as MI, the external input to the excitatory/inhibitory neural populations expected to exhibit altered statistical nature, characterized by temporally correlated afferent drive. To account for this task-dependent modulation of scale-free cortical dynamics, we modified spectral characteristics of the input noise when simulating the MI condition. Specifically, $p(t)$ was modeled as colored noise with a power-law spectrum proportional to $1/(f^k)$, where the exponent k was allowed to vary within the range [0, 1] for all ROIs, sessions, and subjects, and ω is $2\pi f$. We call this modified model as *mi-NMM*.

First, we compared the spectral exponents from the dataset itself to demonstrate that they are different in RS versus MI, therefore justifying our approach to model colored noise in the case of MI. To directly calculate the spectral exponents of all ROIs in both RS and MI conditions, we employed FOOOF, a Python package (43) designed to fit to the power spectra from E/MEG recordings. Firstly, the results showed that FOOOF provided a better fit to the median spectra (calculated by taking the median across all performers for each ROI) than to individual spectra in almost all the sessions/modalities that we considered, based on the R2 metric measuring the goodness-of-fit between the actual spectra and the FOOOF-modeled spectra. For MEG, the mean R2 values for RS condition are 0.983 (median spectra) vs. 0.950 (individual spectra), and for MI condition are 0.990 (median spectra) vs. 0.980 (individual spectra). For EEG, the mean R2 values for RS condition are 0.859 (median spectra) vs. 0.865 (individual spectra), and for MI condition are 0.973 (median spectra) vs. and 0.9118 (individual spectra). This is likely because the median spectra was smoother and therefore, easier to fit to using FOOOF, rather than some of the individual spectra. Note that we used the median instead of the mean when comparing the spectra, as there were few potential outliers that could skew the results (see Fig. S2).

The histogram Fig. 2 shows the spectral exponents in both RS and MI conditions, for the median spectra. Fig. 2: A, B demonstrate that the spectral exponents in the RS condition are smaller than those in the MI condition, when evaluating spectral exponents from the median spectra. However, the histograms for the spectral exponents obtained from the individual spectra shown in Fig. S1(A, B) do not indicate any noticeable difference between the RS and MI conditions. Given that FOOOF fit better to the median spectra, we focused on the result obtained from the median spectra which showed a clear difference in the spectral exponents. Note that a larger spectral exponent can be achieved in our model by incorporating colored noise, while a smaller spectral exponent (capturing the RS condition) can be easily modeled with white noise, as was done in previous studies (19; 18).

Moreover, these empirical observations, especially the task-dependent shift in spectral exponents illustrated in Fig. 2, suggest that the afferent drive to the cortex is not static but changes in nature during task engagement. To test the necessity of modeling this input shift, we performed a control analysis where we modeled both RS and MI with identical input statistics (either both white or both colored). Under these uniform input assumptions, no brain regions exhibited significant task-related modulations for MI versus RS ($p_{\text{FDR}} > 0.05$) for any intrinsic model parameters, despite having strong physiological contrast between the two conditions. In these settings, the intrinsic parameters were effectively forced to absorb the gross

spectral mismatch of the external input between these two conditions, thus masking the subtle task-specific circuit modulations. This indicates that when extrinsic input statistics are constrained to be identical across conditions, the model is unable to disentangle task-related intrinsic parameter changes from the shared input-driven spectral structure. In contrast, allowing the model to incorporate state-dependent input statistics (i.e., the observed exponent shift from RS to MI in empirical analysis), thus approximating extrinsic presynaptic drive as white noise in RS and colored noise in MI – revealed robust and spatially significant ($p_{\text{FDR}} < 0.05$) parameter differences localized to sensorimotor regions (detailed analysis in section 3.3). These regions are known to be directly involved in motor imagery, and the observed parameter modulations were consistent across multiple model parameters. This comparison demonstrates that the observed parameter differences do not arise trivially from changes in the intrinsic spectrum alone; rather, they emerge only when the extrinsic context is accurately modeled. Thus, the spectral/exponents shift represents a fundamental change in the afferent drive which must be explicitly modeled to correctly estimate the intrinsic circuit dynamics described in the following sections. As a result, to capture this shift, we modeled the external input during the MI condition as scale-free brain activity, described by colored noise, reflecting task-dependent modulation of cortical background activity.

3.2 The biophysical mi-NMM captures M/EEG power spectra accurately in both RS and MI conditions

The comparison between the modeled and actual power spectral density (PSD) across different brain regions and sessions reveals a strong correspondence in the decibel (dB) scale over the frequency range of 3 to 30 Hz. The spectral shape of the modeled PSD closely aligns with that of the actual PSD across all examined regions and sessions, demonstrating the effectiveness of the modeling approach in capturing neural oscillatory patterns measured with M/EEG. To demonstrate this qualitatively, example spectra for a subset of regions are shown in Fig. 3 A-D. Here, the regions for RS-modeled EEG, RS-modeled MEG, MI-modeled EEG, and MI-modeled MEG are shown, respectively, demonstrating how the modeled spectral shape aligns with the actual E/MEG spectral shape. A quantitative assessment reinforces these findings, since the Pearson correlation coefficient between the modeled and actual PSD exceeds 0.90 in most cases (Fig. 3 - E, F) in both RS and MI for E/MEG in Session 4. This was also the case for other sessions (Fig. S5 for histograms of other sessions). This high correlation indicates that mi-NMM derived from biophysically realistic parameters' range successfully replicates key spectral features captured via M/EEG in different sessions and regions.

3.3 BCI training drives a shift from diffuse to targeted sensorimotor activation via regional E/I dynamics

The neurophysiologically meaningful model parameters reflect the underlying E/I population-level dynamics that shape how and when a region becomes active in response to internal or external inputs under different conditions. Thus, to investigate the possible condition related modulation/effect for MI versus RS, we conducted the Wilcoxon test for each of these parameters separately in each session (see Fig. S6, $p_{\text{FDR}} < 0.05$). We first examined the spatial distribution of significant brain regions in MEG - associated with three parameters: g_{ei}, g_{ii}, and τ_{e}, with a focus on shift in activation patterns grouped by lobe (see Fig. 4). For an exhaustive presentation of the regions that showed significant effects, please refer to the supplementary table (Table S1) with the list of significant regions of interest (ROIs), session by session for each of these parameters.

Involvement of motor regions As subjects were instructed to perform motor imagery tasks, our primary interest was to investigate the potential involvement of motor areas. For g_{ii}, which reflects self-inhibitory neural gain within the inhibitory population, the *right postcentral gyrus* was found to be significant by session 4. The parameter τ_{e}, which characterizes the duration of the excitatory neural response, yielded the most extensive and consistent activation patterns across sessions with the recruitment of the *paracentral*, the *precentral*, and the *postcentral* gyri during the training. In particular, the left *paracentral* gyrus where we observed a consistent condition effect, also showed a significant training effect across time without correction for multiple testing (Friedmann test, uncorrected $p < 0.05$, Bonferroni adjusted $p = 0.0904$). More specifically, such an effect was driven by the MI condition (see Fig. 5). This finding is particularly important, as the left paracentral region plays a crucial role in the voluntary motor activity of right hand grasping, making it functionally significant in motor control. This change suggests that neural activity in the left paracentral region is dynamically influenced between sessions during motor imagery tasks. Additionally, our mixed-effects modeling analysis revealed a positive correlation between the excitatory time constant (τ_{e}) and group-level BCI performance during motor-imagery condition (Mixed-model: β = 0.38, uncorrected $p <$ 0.05) in the left precentral cortex, a motor region displaying consistent condition-related modulation across sessions. This indicates a positive co-variation between the τ_{e} and group-level BCI performance metrics in the precentral motor area across sessions, after accounting for repeated measurements. This observation is noteworthy given the established role of precentral motor area in motor imagery and BCI control. Our results suggest that the excitatory time constant reliably captures the motor regions' constant involvement in BCI learning thorough E/I population level dynamics. Across sessions, all six motor areas consistently exhibited significant task-related modulation of model parameters during motor-imagery.

Involvement of non-motor regions With non-motor regions, we observed the involvement throughout the training, beyond those targeted by the BCI system. With g_{ei} parameter that plays key role in stabilizing excitatory signals, effects were exclusively observed in session 1. Such brain regions were located in the frontal lobe (left *pars opercularis*), in the parietal lobe (right *inferior* and *superior parietal cortices*), and in the occipital lobe (left *lateral occipital*). For g_{ii}, the bilateral *transverse temporal* cortex were involved through the training. The activations of the other lobes occurred only in session 3 before vanishing in session 4. They involved a reduced number of regions of the frontal (left *rostral middle frontal*), the parietal (left *inferior parietal* cortex and the right *posterior cingulate*), and occipital lobes (left *lateral occipital* cortex). The parameter τ_{e} again yielded the most extensive and consistent activation patterns across the lobes and across training. In the frontal lobe, the left *pars opercularis* was consistently involved until the last session. The other lobes showed consistent activations in all four sessions: in the parietal lobe (the *supramatrarginal* gyrus bilaterally), the *inferior parietal* cortex, the *superior parietal* gyrus, the *precuneus*, and the *posterior cingulate*); the temporal lobe (*transverse temporal*); and in the occipital lobes (the *cuneus* and the *pericalcarine* cortex). Moreover, the distribution of non-motor regions exhibiting significant activation shifted from 24 regions in session-1 to only 14 most relevant non-motor regions by session-4.

Therefore, these findings reveal significant session-by-session differences in brain activity between MI and RS conditions. Notably, differential activation patterns were observed across key sensory, motor, and cognitive processing regions across sessions. Specifically, the parameters g_{ei} and g_{ii} exhibited lower values during RS compared to MI across sessions, whereas τ_{e} demonstrated reduced values in MI relative to RS. These results highlight the dynamic and task-dependent modulation of brain activation patterns in MI compared to RS.

Together, these MEG-derived session-wise changes as illustrated in Fig. 4, indicates a learning-related refinement of cortical engagement, whereby early diffuse activation progressively converges onto task-relevant

sensorimotor regions through region-specific modulation of neuronal population dynamics. Finally, the number of significantly ($p_{\text{FDR}} < 0.05$) activated regions declined from 29 in session 1 to 19 in session 4, reflecting a transition from diffuse to more targeted sensorimotor activation with training. This progressive reduction in spatial extent of activation is robustly captured by the excitatory time constant τ_{e}. Similar analyses were performed on EEG modeled data (refer to the supplementary document).

3.4 Even-related desynchronization and synchronization is associated with model derived reduced excitatory time constant

Event-related desynchronization (ERD) and synchronization (ERS) during motor imagery are characterized by distinct spectral signatures: ERD manifests as a reduction in alpha and beta frequency power, i.e. negative ERD/S (indicating regional activation), whereas ERS reflects sustained or increased oscillation, i.e. positive ERD/S (indicating inactivation). To link these established physiological phenomena to model-derived parameters, we examined whether regions exhibiting ERD/S showed systematic changes in the excitatory time constant (τ_{e}) and neural gains (g_{ei}, g_{ii}) during MI compared to RS. ERD/S was quantified from empirical spectra as the decibel (dB) change in band-limited α (8-12 Hz) and β (13-30 Hz) power between MI and RS ($10\log_{10}(\frac{P_{MI}}{P_{RS}})$), summarized using a composite $\alpha - \beta$ ERD/S measure.

Therefore, first, to assess the global association between ERD/S and model derived parameters, we computed the relative change in τ_{e} for each subject, region and session as $\Delta\tau_{\text{e}}$ (MI/RS-1) between MI and RS. Across regions, ERD/S exhibited a robust positive association with $\Delta\tau_{\text{e}}$ for any given session (Spearman's correlation $\rho : 0.41 \leq \rho \leq 0.55$, all four sessions $p < 0.0005$) (Fig. 6), indicating a consistent global relationship between oscillatory power changes and excitatory population dynamics. Notably, regions that exhibited significant activation in our condition-effect analysis (Section 3.3) also exhibited desynchronization – ERD (negative ERD/S), whereas inactivated regions predominantly exhibited ERS (positive ERD/S), consistent with the well-established functional distinction between ERD and ERS, and clearly illustrated in Fig. 6, where activated regions are in the negative quadrant and inactivated regions are in the positive quadrant. Thereafter, we analyzed the spatial distribution of ERD/S for each of the 68 cortical regions to assess the coupling between longitudinal changes in oscillatory power (ERD/S) and excitatory population dynamics within subject (intra-subject), after accounting for non-independence of training sessions. Repeated-measures correlation analysis revealed a robust within-subject association between $\Delta\tau_{\text{e}}$ and ERD/S in several cortical regions. The association varied regionally, from negative to positive association ($-0.57 \leq r \leq 0.57$) as shown in the brain plot in Fig. 7. The gradient brain plot reveals direction and magnitude of association, where the left superior parietal cortex shows significant positive association ($r = 0.577, p_{\text{FDR}} = 0.00014$), which is known to be involved in motor-imagery and working memory. The scatter plot in Fig. 7, shows session-to-session reductions in τ_{e} during MI were consistently accompanied by stronger desynchronization (negative ERD/S) within individual subjects in the left superior parietal cortex. This significant positive association reveals that, with reduction in excitatory time constant at the population level, there is reduction in $\alpha - \beta$ oscillatory power and vice versa.

We next examined whether ERD/S was associated with changes in neural gains globally. ERD/S exhibited a significant negative association with the E/I coupling neural gain g_{ei} for any given session from session 1 to 3 (Spearman's correlation $\rho : -0.48 \leq \rho \leq -0.42$, all $p < 0.0002$). This negative association indicates that regions showing stronger desynchronization (more negative ERD/S change) were characterized by increased g_{ei}. Mechanistically, this suggests that increased excitatory drive onto inhibitory populations enhances local inhibition, thereby supporting $\alpha - \beta$ oscillation desynchrony. Conversely, regions showing synchronization (positive ERD/S change) were characterized by a relative decrease in g_{ei}, reflecting a regime where excitation dominates local dynamics to sustain resonant oscillations. Importantly, this association

weakened and lost significance by session 4 ($p > 0.05$). The self-inhibitory neural gain g_{ii} showed a weaker and inconsistent association, suggesting a secondary or modulatory role for self-inhibitory coupling in task-related desynchronization. This contrast highlights that while neural gains changes may contribute to ERD/S during early task performance, the reduction in τ_{e} represents a more fundamental and stable physiological signature of the desynchronized state.

Together, these findings demonstrate that ERD/S during MI is underpinned by coordinated reconfigurations in E/I population dynamics. Stronger desynchronization is primarily driven by faster excitatory postsynaptic population responses (reduced τ_{e}). Thus, these global and local association positions τ_{e} as a robust population-level correlate for task-related desynchronization dynamics, embedded within a broader reconfiguration of E/I interactions during motor-imagery.

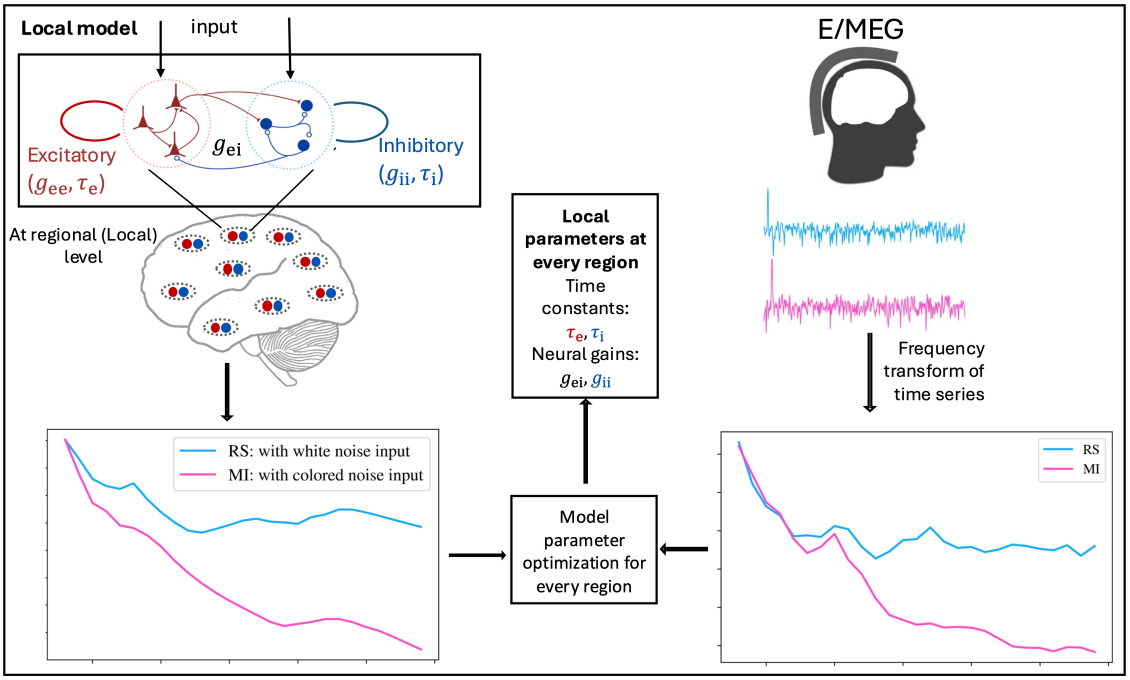

Figure 1: **Workflow for the modeling approach:** On the left, we show that the excitatory and inhibitory neuronal populations are modeled for every brain region using a small set of biophysically meaningful parameters. Both these populations also receive an input that is simulated as white noise for resting state (RS) and colored noise for motor imagery (MI). Upon simulating the model, we directly obtain the power spectral density (PSD) shown at the bottom left. We optimize for the model parameters (shown in the middle) by matching the modeled PSD to the E/MEG PSD for every region, shown in the right most column. After obtaining the optimized parameters, we performed statistical analyses to test for condition and session effect in both E/MEG separately.

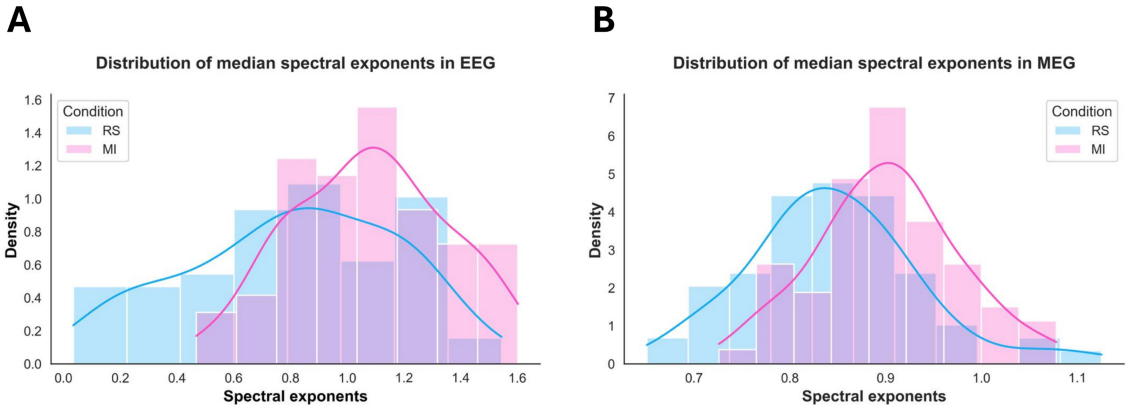

Figure 2: **Task-dependent shift in spectral exponents from Rest (RS) to motor-imagery (MI).** (A, B) exhibit histograms of median spectral exponents in both the conditions and show that the mean of total exponents in RS is lower than in MI in both EEG and MEG, respectively. Compared to RS, MI exhibits a systematic shift toward larger spectral exponents in both modalities, indicating task-dependent modulation of scale-free cortical dynamics.

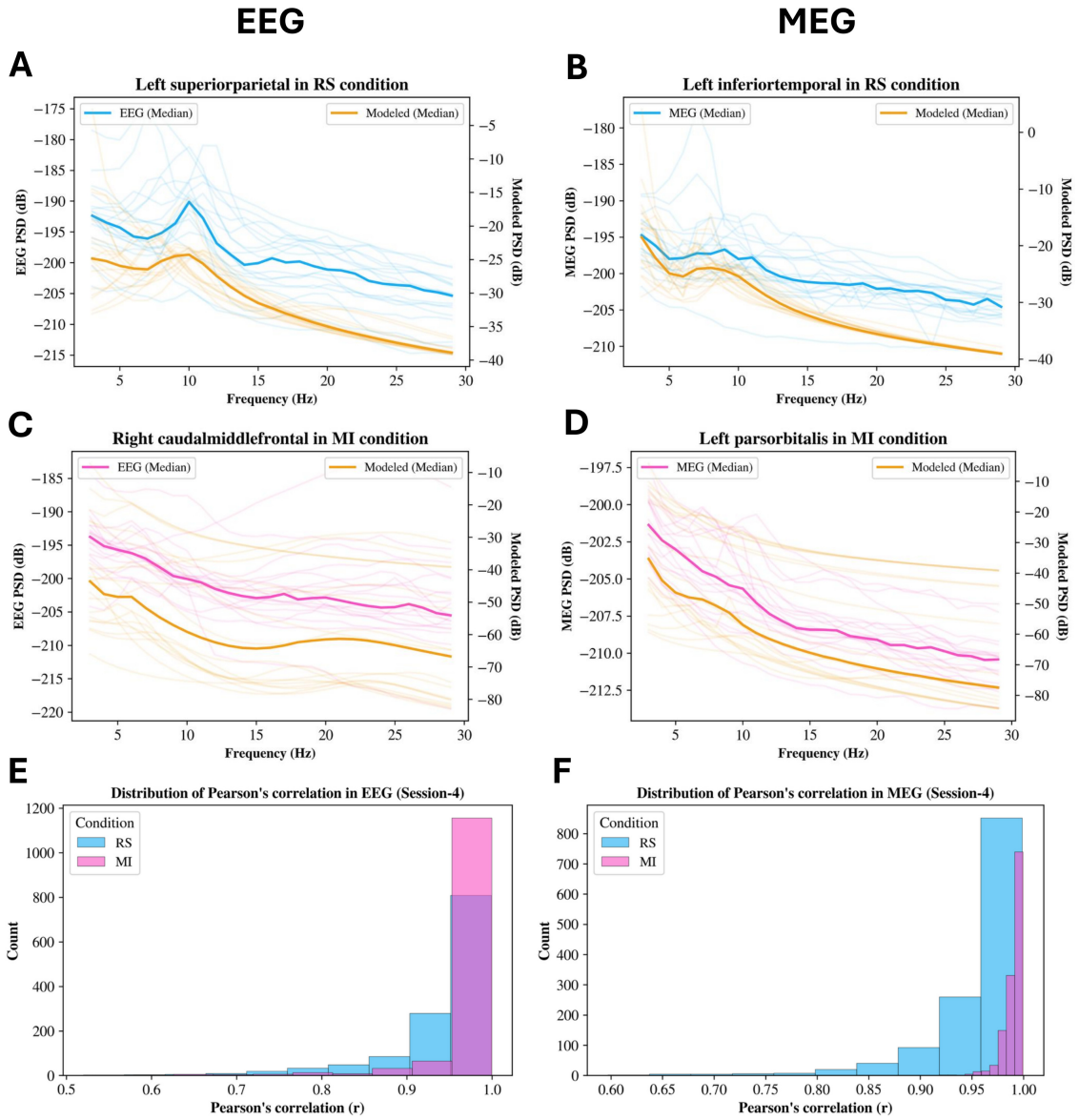

Figure 3: **Matching shape of modeled and actual PSD from M/EEG with Pearson correlation coefficient in both RS and MI.** (A, B): These plots show the modeled PSD compared to the actual EEG and MEG PSDs (in dB scale) for the RS condition, in the left superior parietal and inferior temporal regions, respectively. Each spectra represents data from one of the 19 subjects, while the bold-colored lines represent the median PSDs (modeled and actual). The overlap between these median curves highlights how well the model captures the shape of the actual spectral data; (C, D): Similar to (A, B), but for the MI condition in the right caudal middle frontal and left pars orbitalis regions, respectively; (E, F): These plots show the distribution of Pearson correlation coefficients between the modeled and actual PSDs for session 4, comparing the MI (red) and RS (blue) conditions for EEG and MEG, respectively. A higher correlation indicates better shape matching between the modeled and actual spectra.

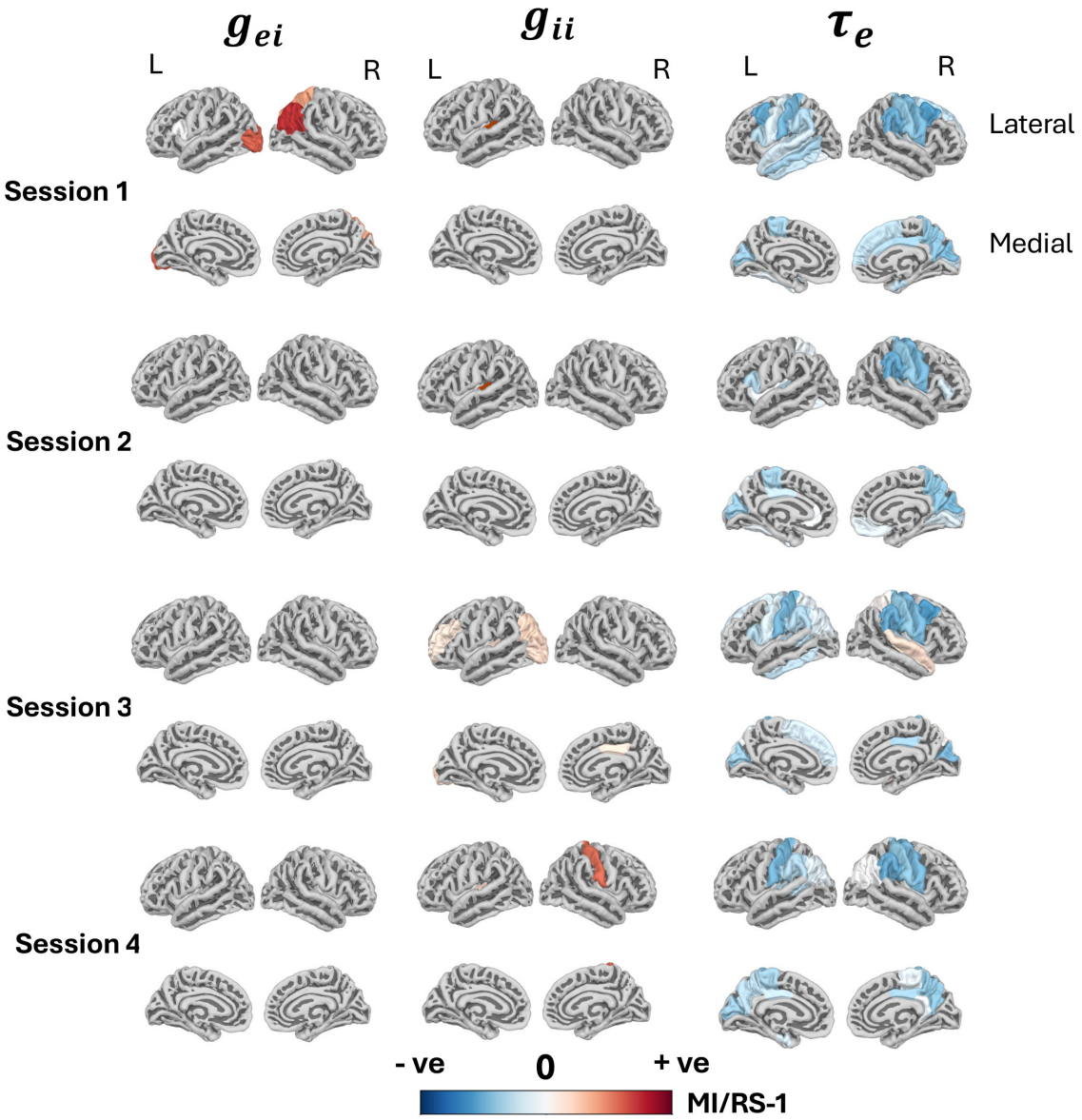

Figure 4: **MEG – Session-wise refinement of cortical recruitment during BCI Learning.** The highlighted colored regions, described by mean (MI/RS-1) across subjects, show statistically significant ($p_{\text{FDR}} < 0.05$) condition effect for MI Vs RS for the three MEG fitted model parameters (g_{ei}, g_{ii}, τ_{e}), respectively, across the four training session. Early training sessions exhibit widespread and distributed cortical involvement, whereas later session show more selective engagement of task-relevant sensorimotor regions, robustly captured by excitatory time constant τ_{e}. This progressive reduction in spatial extent reflects a shift from diffuse to targeted cortical recruitment with training, reflecting functional reorganization across sessions for the MI-BCI task. The minimum and maximum range of mean (MI/RS-1) for the parameters across sessions are (-0.42, +158.47), (+1.95, +336.08), (-0.354, +0.628) for (g_{ei}, g_{ii}, τ_{e}) respectively.

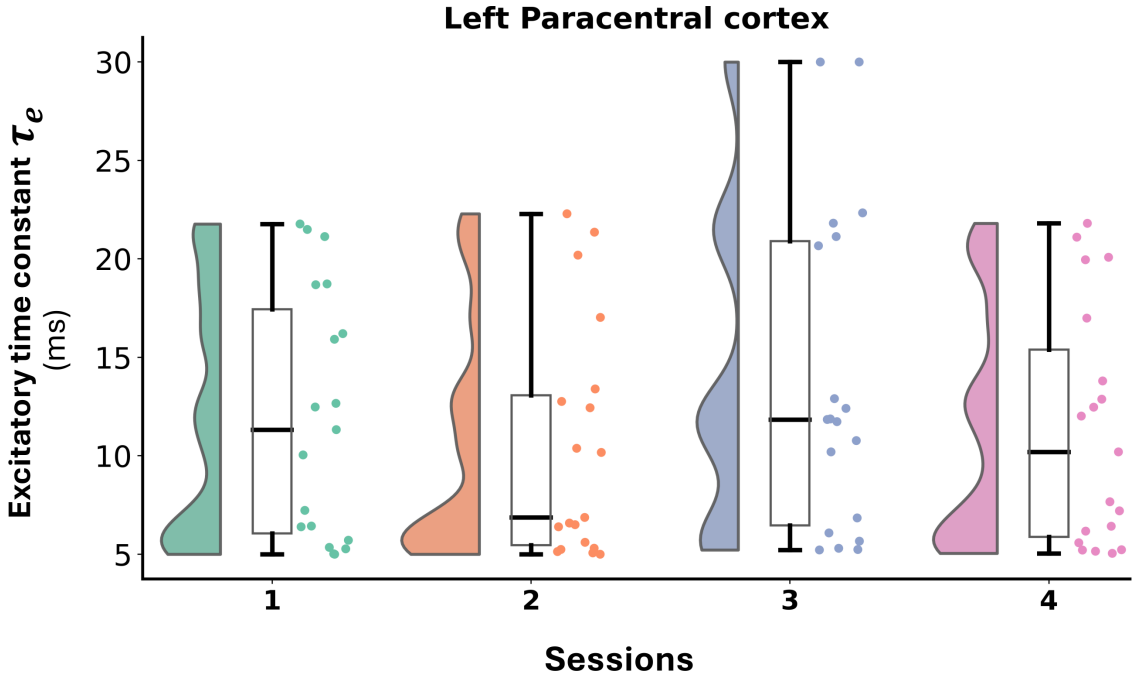

Figure 5: **Variation in excitatory time constant τ_e (ms) is driven by MI condition.** Distribution of 19 individual subject's τ_e values from MEG modeled spectra in each session show inter-session variation in the left paracentral region during MI. Substantial variation across sessions has been observed due to MI (uncorrected $p = 0.0452$; Bonferroni adjusted $p = 0.0904$), indicating session effect driven by MI on group performance in BCI learning.

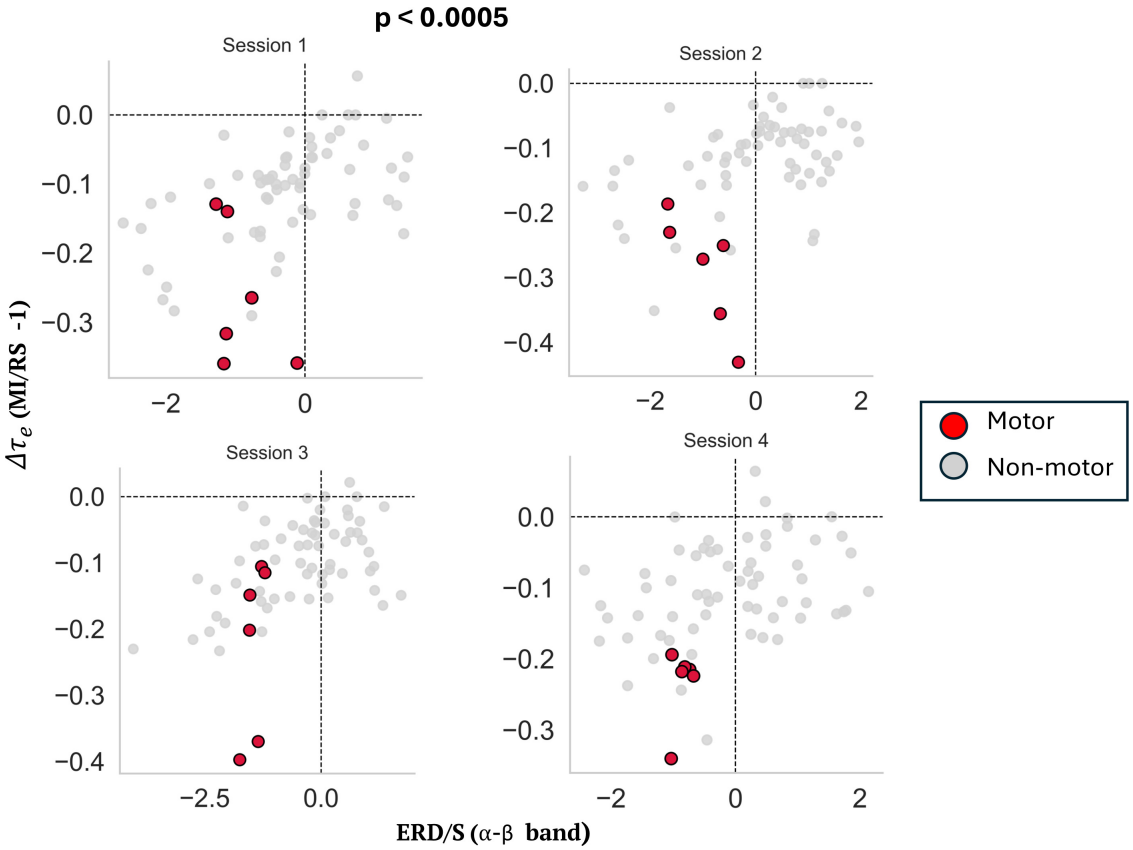

Figure 6: **Significant positive association between reduced excitatory time constant τ_e and ERD/S at the global level.** ERD/S shows siginificant positive association with $\Delta\tau_e$ at the global level in any given session (Spearman's correlation $\rho : 0.41 \leq \rho \leq 0.55$, all sessions $p < 0.0005$). In each of the subplots, each point represents one ROI (median across subjects); motor regions are highlighted. Motor areas consistently exhibited negative ERD/S (red) in all sessions, reflecting event-related desynchronization and task-related activation. These activated regions' transition from synchronized idling state during RS to a desynchronized state during MI, consistent with reduced rhythmic synchronization and faster excitatory population dynamics during active processing.

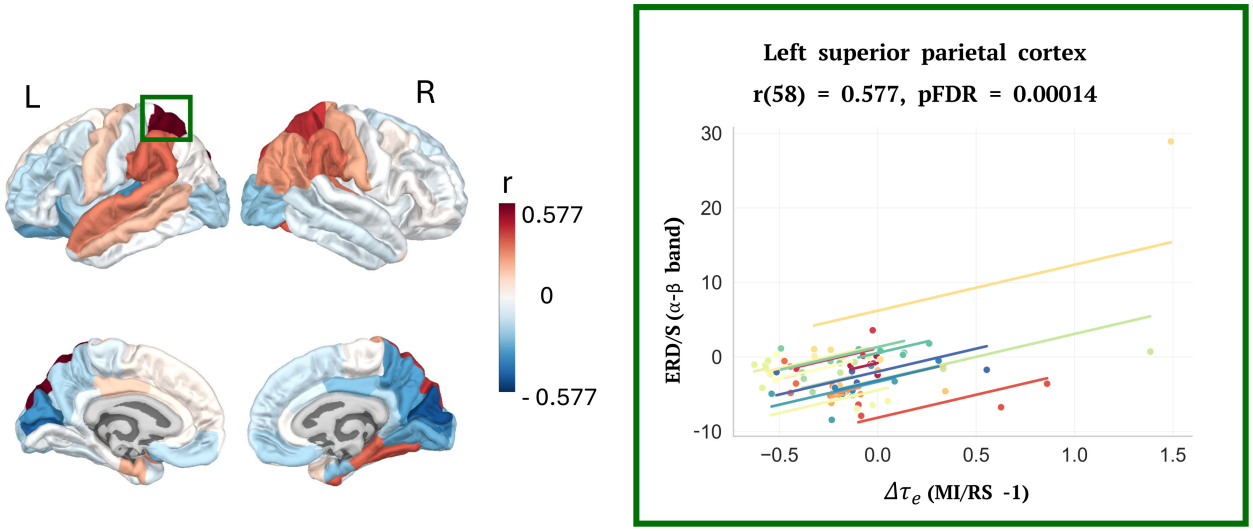

Figure 7: **Within subject association co-variation between ERD/S and reduced excitatory time constant τ_{e} in all brain regions.** Brain map (left) shows variation in repeated measure correlation coefficient (r) between ERD/S and $\Delta\tau_{\mathrm{e}}$ within subjects, across sessions computed for each of the 68 cortical regions. The map reveals both direction and magnitude of the association, r across regions, with warm and cool colors indicating positive and negative association, respectively. The scatter plot (right) illustrates an important cortical region, involved in MI – left superior parietal cortex – showing a significant positive within-subject association between ERD/S and $\Delta\tau_{\mathrm{e}}$ across sessions, and each line represent a subject-specific regression slopes $(n = 19, p_{\mathrm{FDR}} < 0.0002, r = 0.577)$. The robust positive correlation $(r = 0.577)$ indicate that stronger event-related desynchronization (reduction of $\alpha - \beta$ power) is consistently associated with larger reductions in τ_{e} during MI.

4 Discussion

This work represents the first biophysical modeling study in the field of BCI research to use a linear NMM for simulating motor task-related MI data, by modulating the color of the noise in the input signal to the excitatory/inhibitory neuronal populations. Using this novel modeling approach of mi-NMM to simulate MI versus RS, we successfully captured E/MEG spectra of individual brain regions during both conditions. Our findings demonstrate that this approach not only effectively models the MI and RS condition but also identifies key brain regions activated in MI across different BCI training sessions. In doing so, we provide new insights into the neural mechanisms underlying BCI training, paving the way for potential improved interpretability and optimization of BCI systems.

4.1 Comparisons with previous models and neurophysiological grounding of input noise

One important point of discussion is whether using a linear instead of a non-linear model is justified in this case. The key advantage of using a linear model is that we can compute the PSD directly and then compare it with the real data. This reduces the computational load substantially and allows for a wider search of optimal model parameters. Biophysically, it is unclear which model captures the empirical features correctly. However, prior evidence suggests that a linear model may be sufficient in many cases. Most prominently, linear models outperformed non-linear models in predicting resting-state fMRI time series, owing to the linearizing effects of macroscopic neurodynamics and neuroimaging due to spatial and temporal averaging, observation noise, and high dimensionality (44).

A critical aspect of our modeling approach is the external input/stimulus, which we define as aggregate extrinsic pre-synaptic input/background activity arising from distant cortical/sub-cortical regions. In the RS condition, this background activity is considered to be largely asynchronous and weakly correlated across neuronal populations. Thus, under this condition it is considered to be white Gaussian noise. In contrast, during MI condition, we posited that these extrinsic inputs are no longer purely asynchronous. Task engagement recruits coordinated activity across functional networks, leading to temporally structured and correlated afferent drive. Thus, to capture this regime, we modeled this external input as colored noise with a power-spectrum proportional to $1/(f^k)$. Moreover, this modeling approach is neurophysiologically grounded in the framework of scale-free brain dynamics. Previous studies on scale-free brain activity (12; 13) demonstrated that the background arrhythmic activity of the brain, which often treated as noise, exhibit a robust $1/f$ temporal structure that is functionally significant, contributing actively to brain functioning. According to these developments, scale-free brain activity in noninvasive recordings like EEG and MEG offers a window into the population level activity of cortical pyramidal neurons rather than being a typical noise. They showed that the exponent of this scale-free activity is not static but is systematically modulated by task demands, reflecting shifts in brain's functional operating point that facilitates information processing. Therefore, to capture this task-induced modulation in arrhythmic brain activity, we use colored noise for the MI task condition.

However, all the non-linear NMM (40; 41; 42; 15) as well as the limited modeling studies that have been done previously using non-linear NMMs to model motor tasks have attempted to capture task effects by adjusting the mean and variance of the white noise input (which is used to simulate RS). For instance, in (16), where the motor task involved grasping a pressure sensor with the right hand to measure grip strength, the mean and standard deviation of the Jansen-Rit model's white noise parameter were adjusted to fit to the alpha band EEG power spectral density data. Similarly, in (15), where data were recorded during right-hand finger movements and the execution of a working memory task, the Wendling et al. (45) NMM was modified by incorporating white noise with a defined mean and variance. The mi-NMM consists of a linear NMM

in which the noise parameter remains white noise with a constant mean and variance in RS. However, for the MI-BCI task, we assumed the input to be colored noise. This is because unlike non-linear neural mass models, simply changing the mean and variance of the white noise will not change the shape of the PSD – it will only modify the amplitude. Therefore, we needed to modify the color of the noise in our case. Our empirical results (Section 3.1) Fig. 2 demonstrate clear task-dependent changes in spectral exponents during MI, supporting this hypothesis. By transitioning the input from white to colored noise, the mi-NMM provides a mechanistic account of this modulation, capturing a shift from asynchronous background drive in RS to temporally structured task-driven input during MI.

4.2 Relevance of mi-NMM parameters in motor task

The mi-NMM we used here allows us to relate the model's parameters to the neurophysiological functions of the cerebral cortex. This is especially true for the motor cortex, which was recorded by both EEG and MEG during the right-hand grasping motor imagery task. By fine-tuning these model parameter values within a biophysically realistic range, we were able to closely match the PSD shapes of the E/MEG and modeled spectra. This allowed us to further investigate the link between the physiological mechanisms underpinning BCI training and the neurophysiologically meaningful model parameters.

Importantly, the reduced excitatory time constant (τ_{e}) during MI compared to RS across sessions is consistent with the well-established phenomenon of ERD/S in the alpha and beta frequency bands (46). Physiologically, active processing places neurons in a high-conductance state, characterized by a reduction in effective membrane time constants due to increased synaptic drive and low resistance (47). Within the mi-NMM framework, this physiological regime is reflected at the local population level as a faster decay of excitatory responses (reduced τ_{e}), supported by increased E/I coupling neural gain in the functionally activated regions, thereby reducing the capacity to sustain alpha and beta band rhythmic activity (negative ERD/S) as reflected in one of the MI relevant region – left superior parietal cortex in Fig. 7. This way, the model provides a mechanistic bridge between macroscopic ERD/S and its underlying biophysical determinants, consistent with neural mass modeling studies linking synaptic dynamics to oscillatory activity (42).

Moreover, our findings suggest that with each session, the mi-NMM parameters are able to capture the functional reorganization occurring in the cortical regions. Furthermore, with progress in training with a specific focus on MI, it appears that subjects modulate brain rhythmic/arrhythmic activity in relevant motor regions in the alpha and beta frequency bands, which is captured by the model parameters.

By matching the shape of the E/MEG PSD with the modeled PSD from the mi-NMM, we explore the relationship between model parameters and the associated neural mechanisms of BCI training. The findings indicate that the MEG-fitted modeled parameters evolved from session 1 through session 4. The excitatory time scale (τ_{e}) evolved from randomly capturing cerebral cortex regions in session 1 to precisely capturing specific motor and associated regions in session 4 such as: Motor lobe (right precentral, bilateral paracentral) responsible for motor imagery and motor hand tasks (48); Parietal lobe (bilateral inferior parietal, bilateral postcentral, bilateral precuneus, bilateral supramarginal) involved in sustained attention, detection of salient events, memory retrieval and memory processing (49; 50; 51; 52; 53; 54); Occipital lobe (left cuneus, left pericalcarine) associated with visual mental imagery and detection of patterns (55; 56; 57); Limbic regions (right isthmus cingulate, bilateral posterior cingulate) responsible for spatial memory and navigation (58; 59). Similarly, with inhibitory neural gain parameter (g_{ii}), the postcentral region in session 4 engaged in MI BCI task and showed significant condition effect, whereas E/I coupling neural gain parameter (g_{ei}) showed no significant effect in later sessions except session 1.

The EEG-fitted modeled parameters also evolved from session 1 through session 4. Initially, no specific brain regions were captured during the early training sessions. However, by the end of the training, in session 4,

the parameters successfully identified highly relevant regions for the MI-BCI task. This suggests that although subjects were initially naïve, training enabled them to engage the necessary brain regions for BCI. The E/I coupling neural gain parameter (g_{ei}), which showed no significant regional effects in session 1, finely adjusted its values over the course of training. This gradual tuning suggests that the interaction between excitatory and inhibitory neural populations was actively regulated over time, helping certain brain regions become more responsive. Such changes likely reflect a shift toward increased net excitation at the population level, allowing these regions to engage more effectively during task performance. By session 4, it successfully captured critical regions, including: Occipital lobe (bilateral cuneus, left lateral occipital)- involved in visual pattern detection, tracking visual motion, visual memory recognition, and visual mental imagery (55; 56; 57; 60); Parietal lobe (left inferior parietal)-associated with somatosensory processing and spatial awareness (49); Frontal-motor area (left precentral cortex) - responsible for motor control and execution (48). Similarly, with the inhibitory neural gain parameter (g_{ii}), we could observe some important regions (bilateral cuneus, left isthmus cingulate, left lingual, right parahippocampal) involved in spatial memory and navigation, memory formation, episodic memory retrieval, motor detection and tracking (58; 61; 62; 63; 64) show significant condition effect in session 4. Also, the excitatory time scale (τ_{e}) in session 4 showed significant condition effect for supramarginal gyrus, which involved in somatosensory processing task (53; 54).

These observations align with a previous study (16), where NMM parameters successfully captured the underlying mechanisms of motor tasks in EEG. That study employed a single-channel Jansen-Rit (40; 41) NMM at the sensor level, specifically the C3 channel, which corresponds to the primary motor area. In contrast, our study utilizes source-reconstructed recordings from all the regions of cerebral cortex, offering very comprehensive and significantly higher accuracy than sensor-space data. In that study, the effects of average excitatory and inhibitory synaptic gain were analyzed to examine the power spectral density of the model's output signal in the alpha band, while keeping other parameters at typical values. By doing so, they established connections between Jansen-Rit's single-channel NMM parameters and the physiological mechanisms of the motor cortex, particularly by analyzing changes in grip force during a motor task. Their findings demonstrated that as grip force increased, the recruitment of motor neurons in the motor cortex also rose. The model effectively captured these changes in EEG signals by adjusting gain parameters, suggesting that increasing grip force activates more motor neurons in the motor cortex and elevates their firing rate.

4.3 Investigating learning effect with mi-NMM

One of the primary challenges in BCI study is addressing inter- and intra-subject variability (4; 65; 66; 67). Understanding the large-scale neural mechanisms underlying plasticity is essential for elucidating the processes of human learning (68; 69; 70; 71). The voluntary modulation of neural activity to operate a BCI is increasingly regarded as an acquired skill. Numerous studies have demonstrated that performance in BCI tasks typically improves with practice (72; 73; 10). Users often report a transition from explicit, effortful cognitive strategies–such as motor imagery–to more automatic, goal-directed control that closely resembles natural motor execution. This behavioral progression is indicative of procedural motor learning mechanisms being engaged in the brain. To investigate the neural dynamics underlying BCI skill acquisition, researchers have employed neuroimaging methods in both non-human primates (72; 74; 75; 76; 77) and humans (78; 79; 80). These studies suggest that, although BCI control typically relies on modulating activity within motor-related brain areas, a broader and dynamically changing network of cortical regions contribute to the early stages of BCI learning. Other groups have investigated the use of power spectra within theta, alpha, and gamma bands as potential predictors of BCI scores (6; 81; 82), with some difficulties to replicate such observations (83). Such elements explain why the specific mechanisms supporting BCI learning remain poorly understood. Understanding how neural patterns differ across individuals (inter-subject) and within the

same individual across sessions (intra-subject) is crucial for developing robust BCI training programs.

This study aims to enhance specificity at both the individual and regional levels, providing more precise estimates of learning effects in BCI applications and offering deeper insights into the underlying mechanisms. While investigating the effect of MI compared to RS in each session, we analyzed regions of cerebral cortex based on DK atlas independently for each parameter across individuals (inter-subject) in E/MEG. Here, we can observe that with an increase in session the mi-NMM parameters are able to specifically capture various important regions ($p_{\text{FDR}} < 0.05$) that are activated and are responsible for the BCI task. E/I coupling neural gain parameter (g_{ei}), reflecting the functional interaction strength between the excitatory and inhibitory populations, showed significant changes in a limited, yet functionally critical areas in session 1. Specifically, significant regions that got activated as a result include the right inferior parietal cortex which is involved in sustaining attention over time (84); left lateral occipital cortex for visual memory recognition, visual object completion (60); left pars opercularis, and right superior parietal cortex essential for the manipulation of information in working memory and supports executive processes required to rearrange and mentally transform information (85). This initial pattern of activation may serve as a baseline or scaffold that enables subsequent learning as we did not observe any significant regions in other sessions. As participants become more experienced with the BCI task, the neural processes underlying sensory integration and motor planning likely become more efficient, possibly reducing the need for further modulation of the g_{ei} parameter. In other words, although g_{ei} is strongly engaged during the initial performance of the task, its influence appears to stabilize with practice, providing a consistent framework upon which other neural adaptations are reflected in parameters such as g_{ii} and τ_{e}.

With the inhibitory neural gain parameter (g_{ii}) we did not observe motor related or associated area getting activated at the beginning of the training. However, by session 3, increased functional engagement of task-relevant regions may reflect a shift in local population/circuit dynamics, where refined self-inhibitory feedback within the inhibitory neural population reduces the overall inhibitory output, thus decreases its net suppressive influence on excitatory neurons. This disinhibition potentially gives rise to net excitation with greater excitatory activity and allows specific regions to become more functionally responsive during task performance, enhancing the effectiveness of BCI training. Thus, involvement of these areas suggests that as learning progresses, inhibitory gain processes become more distributed across networks including regions involved in sustained attention (inferior parietal and posterior cingulate) (84; 59); and in visual processing (lateral occipital) (60). Such an expansion exhibits the brain's adaptation to more efficiently suppress task-irrelevant inputs (86) and optimize sensorimotor integration during motor imagery. Finally by session 4, the pattern of activation associated with g_{ii} showed very distinct refinement, with significant activity observed in the right postcentral area. The involvement of this region underscores the integration of somatosensory information and the fine-tuning of motor learning, while the continued significance of the left transverse temporal area from session 1 till the end reinforces its role in memory processing. This refined pattern in the final session indicates that with sustained practice, inhibitory gain mechanisms evolve to support more specific functions—namely, enhancing voluntary motor control. Additionally, we observed a decrease in the total number of activated regions from session 1 (29 regions) to session 4 (19 regions). This reduction suggests that, with training, subjects were able to selectively engage the most relevant regions responsible for the MI task, thereby improving their control over the BCI. Such observations are in line with previous findings, where event-related desynchronization was observed as a significant power decrease ($p < 0.025$) in alpha and beta frequency bands. This was observed in cortical regions associated with key cognitive and sensorimotor functions relevant to BCI control, namely (33): sensorimotor integration and motor imagery (superior parietal lobule), decision-making and memory consolitation (middle anterior cingulate gyrus), behavioral adaptation (posterior ventral cingulate gyrus and frontomarginal gyrus), visual tracking (lingual

gyrus), mental rotation and working memory (orbital part of the inferior frontal gyrus).

The excitatory synaptic time scale (τ_e), which represents the duration of neuronal responses in excitatory neuronal sub-populations, is a critical parameter for determining how long excitatory signals persist in a brain region. In our study, τ_e exhibited notable changes in sessions that are indicative of learning-induced neural plasticity during motor imagery. In session 1, τ_e related activity is widely distributed in many regions suggesting that at the beginning of BCI training, the duration of excitatory response are widely distributed, reflecting a generalized and random recruitment of neural circuits involved in sensory processing, higher-order cognition, and motor coordination. By session 2, as learning begins, the activation becomes more focused as reflected by τ_e . Significant effects emerge in regions involved in visual processing and mental imagery (cuneus, and lingual gyrus) (56; 57; 61; 62), error detection (left insula) (87). This indicates an early refinement of the timing of excitatory response, as the brain begins to adapt to the temporal dynamics of the specific motor imagery condition (88). Then, τ_e related activity expanded further to include additional areas such as the left inferior parietal and temporal regions, suggesting that, with continued practice, the duration of the excitatory neural population response is being fine-tuned to support more efficient sensorimotor integration and cognitive processing. Finally, in session 4, τ_e exhibited the most extensive and robust activation pattern, with significant involvement of regions crucial for motor imagery and motor hand tasks (precentral, paracentral and postcentral gyri) (89; 90); for memory processing (precuneus, posterior cingulate, entorhinal cortex) (55; 59; 91); and for sustained attention (inferior parietal and supramarginal regions) (84; 53). We went one step further and investigated the potential training effect in the left paracentral region for MEG-fitted modeled τ_e values during MI. There is a substantial variation in τ_e over time for this region, which also shows a significant effect of condition. This progressive expansion and increased specialization of τ_e between sessions strongly suggest that with repeated practice, the neural circuits underlying the excitatory synaptic time scales become finer tuned. This tuning likely improves the temporal precision of sensorimotor integration, reflecting learning-induced neural plasticity such as functional reorganization as subjects improve their performance during motor imagery tasks. This adaptation is a hallmark of learning, suggesting that repeated motor imagery practice leads to more efficient and targeted excitatory responses in the brain's sensorimotor networks.

4.4 Replicability

In order to further validate our observations, another dataset was brought for analysis. In this dataset, 15 subjects (RH, 8 F) performed a MI task to grasp an object using a robotic arm. They use a combination of gaze to indicate the position to reach and either performed MI of the right hand or resting state to grasp or not the object presented. They actively controlled the robot for 3 runs with 10 trials per condition. The protocols and results of the findings can be found in (92). Among the control strategies used, we only focused on the strategy where the robot moved prior to the MI task as it showed the highest level of desynchronization across subjects previously. In order to reduce variability of the findings due to the processing pipeline, we performed source reconstruction using wMNE and used parcellation with PCA over dipoles to get the Desikan-Killiany atlas in the different conditions of rest and MI. This set of subjects did not have their MRI scan meaning that the inverse method was done using fsaverage (an MRI template on the average of 40 subjects (93)). This means regions involved are to be interpreted cautiously as some of them could be overlapping over points specific to the different subjects.

The dataset revealed a decrease in the PSD in MI with respect to RS in the broad range α-β bands, specifically in the post central region (94; 95) even though the mi-NMM parameters were not significant, contributing to confirm the MI of the right hand taking place in the different subjects. Furthermore, different regions that were mentioned in the previous analysis (96) have significantly different mi-NMM parameters in

MI versus RS, shown in Fig. S8. Among them, we can pin out the caudal middle frontal region (97; 98) and the paracentral region (99) both used for motor planning to facilitate the execution of goal-directed actions and attention allocation which brings up new insights on the robotic involvement in the MI process; and the frontal pole associated with high-level cognitive functions like decision-making (with the limitation that it could be artifacted by gaze activity). The superior parietal lobe was also found to be activated significantly again. This region is found to be a central hub of multisensory integration and spatial perception (100), and is also involved in sense of agency and visuomotor coordination. These findings reinforce previous results on the impact of the robotic arm over subjects in their integration of the device to their mental workspace. Furthermore, our results based on the mi-NMM parameters in this validation dataset show that they can capture activation in the relevant regions as was the case with our main dataset. Other regions that were previously not listed (96) had significantly different mi-NMM parameters in MI – they may be relevant to performing MI such as the pericalcarine and cuneus regions involved in visual processing (101); and the medial orbitofrontal lobe associated with reward processing (102; 103) that may be relevant to the neurofeedback in MI.

An important point of discussion is the reproducibility of the model findings, especially given that the experimental conditions and the tasks performed in the two BCI trainings are completely different. Despite these differences, mi-NMM consistently identified brain regions that overlap as statistically significant ($p_{\text{FDR}} < 0.05$) across the two datasets, suggesting robustness in its ability to capture key neurobiological correlates. Specifically, in the case of the parameter g_{ii} (which reflects the inhibitory gain in inhibitory neural sub-population), two regions emerged as replicable in both datasets. First, the parahippocampal cortex (responsible for episodic memory formation and memory retrieval) was identified in both datasets as a region of significance. This recurrent involvement suggests a stable role of this region in the inhibitory-inhibitory circuit dynamics modeled, possibly reflecting task-general mnemonic processing. Second, the Cuneus region (involved in visual detection of patterns, visual mental imagery and attention modulation) also consistently appeared as significant. This overlap may reflect a shared visual or attentional demand across tasks, even if they differ in cognitive context.

Similarly to the previous dataset, condition effects observed with g_{ii} were associated with lower values in RS compared to MI, whereas τ_{e} exhibited lower values in MI than in RS. Notably, these consistencies between datasets—particularly in the absence of identical experimental conditions—demonstrate the potential generalizability of the mi-NMM and its capacity to identify relevant neurobiological correlates. However, not all parameters exhibited such reproducibility. For instance, g_{ei} and τ_{e} did not yield overlapping regions between datasets, suggesting that parameter-specific effects may be more sensitive to task or dataset characteristics.

4.5 Limitations

The current study consists of several limitations. In this study, the training sessions and number of participants are limited, and future studies replicated in larger, more diverse cohorts will help generalize the findings universally. Currently, with mi-NMM we only tried to match the modeled spectra to the shape of the actual power spectra, not the magnitude. This is because the most prominent change from resting state to MI is in the shape of the spectra, and therefore it is reasonable to focus only on capturing the shape by using the Pearson correlation coefficient as the cost function in the optimization. This also eases the computational burden, since we do not need to estimate the optimal magnitude of the spectra as an additional parameter.

An interesting observation from our analysis of EEG and MEG data is the behavior of the fitted model parameter τ_{e}. In EEG, τ_{e} does not show any condition effect or capture any region except one in session 4, making it difficult to pinpoint specific areas of activity for this parameter. However, in MEG, τ_{e} reliably highlights regions within the cerebral cortex during all four sessions, suggesting that MEG provides a more

stable and regionally specific representation of neural dynamics compared to EEG. Similar to the findings in our previous study (33), a greater number of regions of interest exhibited significant condition effects in MEG compared to EEG. This discrepancy can be attributed to the distinct biophysical properties of the two modalities. EEG signals are attenuated by the varying conductivities of intervening tissues, such as the scalp, skull, and cerebrospinal fluid (104), and are sensitive to both tangential and radial components of cortical dipoles. In contrast, MEG offers superior spatial resolution and is primarily sensitive to the tangential components of neural sources (105). Consequently, EEG and MEG do not necessarily capture the same aspects of brain activity. Furthermore, participants were instructed to lean their heads back within the MEG helmet during data acquisition. This positioning brought the MEG sensors closer to the parietal and occipital regions, potentially enhancing the sensitivity to posterior brain activity relative to signals arising from the frontal areas.

5 Conclusions

Despite the fact that BCI is no longer an emerging field, the mechanisms involved in training to master the control are too often examined solely through the lens of performance, without adequately addressing the brain's intrinsic dynamics. One key aspect in the adoption of BCIs – particularly in motor imagery paradigms – is understanding how E/I coupling mechanisms unfold. Models previously describing E/I coupling have been mostly applied to resting-state data where the input to the E/I neuronal populations is assumed to be background non-specific noise and therefore approximated by Gaussian noise. BCI tasks rely on active engagement such as motor imagery. Our work addresses this gap by extending existing modeling approaches to account for task-driven activity.

Our results show that, once fine-tuned, mi-NMM is capable of replicating task dynamics across sessions in a way that closely mirrors real data. Its ability to track session-to-session variations provides compelling evidence that E/I coupling may play a role as an underlying brain mechanism during BCI learning. Furthermore, mi-NMM successfully captures differences between tasks across modalities (EEG, MEG) and experimental conditions–whether the BCI feedback was provided via a screen (visual feedback) or through a robotic arm (embodied feedback). These additional findings strengthen the robustness of the observed effects and lend credibility to the overall approach.

Looking ahead, these insights open the door to integrating E/I coupling into the BCI framework, as it emerges as a relevant feature in shaping and informing the training process. More broadly, embedding these mechanisms into BCI design could contribute to more refined and neurobiologically grounded models, ultimately enriching both the theoretical and practical aspects of BCI development.

Availability of materials

All the codes related to the paper can be found on this Github page:
https://github.com/ApurbaApd/mi-NMM_bci_modeling

Funding

The authors acknowledge support from Transatlantic Research Partnership from the FACE Foundation and Alzheimer's Association grant AARFD-22-923931 and support from the European Research Council (ERC), Grant Agreement No. 864729.

Supplementary material

Please see the supplementary document for the additional information.

References

[1] M. Clerc, L. Bougrain, and F. Lotte, *Brain-Computer Interfaces 1: Methods and Perspectives*. Wiley, wiley ed., 2016.

[2] M. Clerc, L. Bougrain, and F. Lotte, *Brain-Computer Interfaces 2: Technology and Applications*. Wiley, wiley ed., 2016.

[3] J. J. Shih, D. J. Krusienski, and J. R. Wolpaw, "Brain-Computer Interfaces in Medicine," *Mayo Clinic Proceedings*, vol. 87, pp. 268–279, Mar. 2012.

[4] B. Z. Allison and C. Neuper, "Could anyone use a BCI?," in *Brain-Computer Interfaces* (D. S. Tan and A. Nijholt, eds.), Human-Computer Interaction Series, pp. 35–54, Springer London, 2010.

[5] F. Lotte, L. Bougrain, A. Cichocki, M. Clerc, M. Congedo, A. Rakotomamonjy, and F. Yger, "A review of classification algorithms for eeg-based brain-computer interfaces: a 10 year update," *Journal of Neural Engineering*, vol. 15, no. 3, p. 031005, 2018.

[6] M. Ahn and S. C. Jun, "Performance variation in motor imagery brain–computer interface: A brief review," *Journal of Neuroscience Methods*, vol. 243, pp. 103–110, Mar. 2015.

[7] O. Alkoby, A. Abu-Rmileh, O. Shriki, and D. Todder, "Can We Predict Who Will Respond to Neurofeedback? A Review of the Inefficacy Problem and Existing Predictors for Successful EEG Neurofeedback Learning," *Neuroscience*, vol. 378, pp. 155–164, May 2018.

[8] S. C. Kleih, F. Nijboer, S. Halder, and A. Kübler, "Motivation modulates the p300 amplitude during brain-computer interface use," *Clinical Neurophysiology*, vol. 121, no. 7, pp. 1023–1031, 2010.

[9] C. Jeunet, E. Jahanpour, and F. Lotte, "Why standard brain-computer interface (bci) training protocols should be changed: an experimental study," *Journal of Neural Engineering*, vol. 13, no. 3, p. 036024, 2016.

[10] R. Sitaram, T. Ros, L. Stoeckel, S. Haller, F. Scharnowski, J. Lewis-Peacock, N. Weiskopf, M. L. Blefari, M. Rana, E. Oblak, N. Birbaumer, and J. Sulzer, "Closed-loop brain training: the science of neurofeedback," *Nature Reviews Neuroscience*, vol. 18, no. 2, pp. 86–100, 2017.

[11] D. S. Bassett, N. F. Wymbs, M. A. Porter, P. J. Mucha, J. M. Carlson, and S. T. Grafton, "Dynamic reconfiguration of human brain networks during learning," *Proceedings of the National Academy of Sciences of the United States of America*, vol. 108, no. 18, pp. 7641–7646, 2011.

[12] B. J. He, J. M. Zempel, A. Z. Snyder, and M. E. Raichle, "The temporal structures and functional significance of scale-free brain activity," *Neuron*, vol. 66, no. 3, pp. 353–369, 2010.

[13] B. J. He, "Scale-free brain activity: past, present, and future," *Trends in Cognitive Sciences*, vol. 18, no. 9, pp. 480–487, 2014.

[14] M. Breakspear, "Dynamic models of large-scale brain activity," *Nature neuroscience*, vol. 20, no. 3, pp. 340–352, 2017.

[15] M. Zavaglia, L. Astolfi, F. Babiloni, and M. Ursino, "A neural mass model for the simulation of cortical activity estimated from high resolution eeg during cognitive or motor tasks," *Journal of Neuroscience Methods*, vol. 157, no. 2, pp. 317–329, 2006.

[16] Y. Zhang, Z. Li, H. Xu, Z. Song, P. Xie, P. Wei, and G. Zhao, "Neural mass modeling in the cortical motor area and the mechanism of alpha rhythm changes," *Sensors (Basel, Switzerland)*, vol. 25, no. 1, p. 56, 2024.

[17] A. Raj, C. Cai, X. Xie, E. Palacios, J. Owen, P. Mukherjee, and S. Nagarajan, "Spectral graph theory of brain oscillations," *Human Brain Mapping*, vol. 41, no. 11, pp. 2980–2998, 2020.

[18] P. Verma, S. Nagarajan, and A. Raj, "Spectral graph theory of brain oscillations–revisited and improved," *NeuroImage*, vol. 249, p. 118919, 2022.

[19] K. G. Ranasinghe, P. Verma, C. Cai, X. Xie, K. Kudo, X. Gao, H. Lerner, D. Mizuiri, A. Strom, L. Iaccarino, R. La Joie, B. L. Miller, M. L. Gorno-Tempini, K. P. Rankin, W. J. Jagust, K. Vossel, G. D. Rabinovici, A. Raj, and S. S. Nagarajan, "Altered excitatory and inhibitory neuronal subpopulation parameters are distinctly associated with tau and amyloid in alzheimer's disease," *eLife*, vol. 11, p. e77850, 2022.

[20] J. M. Fan, K. Kudo, P. Verma, K. G. Ranasinghe, H. Morise, A. M. Findlay, K. Vossel, H. E. Kirsch, A. Raj, A. D. Krystal, *et al.*, "Cortical synchrony and information flow during transition from wakefulness to light non-rapid eye movement sleep," *Journal of Neuroscience*, vol. 43, no. 48, pp. 8157–8171, 2023.

[21] J. R. Wolpaw, D. J. McFarland, T. M. Vaughan, and G. Schalk, "The wadsworth center brain-computer interface (bci) research and development program," *IEEE Transactions on Neural Systems and Rehabilitation Engineering*, vol. 11, no. 2, pp. 204–207, 2003.

[22] S. Taulu and J. Simola, "Spatiotemporal signal space separation method for rejecting nearby interference in meg measurements," *Physics in Medicine and Biology*, vol. 51, no. 7, pp. 1759–1768, 2006.

[23] A. J. Bell and T. J. Sejnowski, "An information-maximization approach to blind separation and blind deconvolution," *Neural Comput*, vol. 7, no. 6, pp. 1129–1159, 1995-11.

[24] R. Oostenveld, P. Fries, E. Maris, J.-M. Schoffelen, R. Oostenveld, P. Fries, E. Maris, and J.-M. Schoffelen, "FieldTrip: Open source software for advanced analysis of MEG, EEG, and invasive electrophysiological data," *Computational Intelligence and Neuroscience*, vol. 2011, p. e156869, 2010-12.

[25] M. Fuchs, M. Wagner, and J. Kastner, "Boundary element method volume conductor models for EEG source reconstruction," *Clinical Neurophysiology*, vol. 112, no. 8, pp. 1400–1407, 2001.

[26] A. Gramfort, T. Papadopoulo, E. Olivi, and M. Clerc, "OpenMEEG: opensource software for quasistatic bioelectromagnetics," *BioMedical Engineering OnLine*, vol. 9, p. 45, 2010.

[27] M. Fuchs, M. Wagner, T. Köhler, and H. A. Wischmann, "Linear and nonlinear current density reconstructions," *Journal of Clinical Neurophysiology: Official Publication of the American Electroencephalographic Society*, vol. 16, no. 3, pp. 267–295, 1999-05.

[28] F.-H. Lin, T. Witzel, S. P. Ahlfors, S. M. Stufflebeam, J. W. Belliveau, and M. S. Hämäläinen, "Assessing and improving the spatial accuracy in MEG source localization by depth-weighted minimum-norm estimates," *Neuroimage*, vol. 31, no. 1, pp. 160–171, 2006-05.

[29] A. Gramfort, M. Luessi, E. Larson, D. A. Engemann, D. Strohmeier, C. Brodbeck, L. Parkkonen, and M. S. Hämäläinen, "MNE software for processing MEG and EEG data," *NeuroImage*, vol. 86, pp. 446–460, 2014-02-01.

[30] F. Tadel, S. Baillet, J. Mosher, D. Pantazis, and R. Leahy, "Brainstorm: A user-firendly application for MEG/EEG analysis," *Computational Intelligence and Neuroscience*, vol. 2011, 2011-01.

[31] J. C. Mazziotta, A. W. Toga, A. Evans, P. Fox, and J. Lancaster, "A probabilistic atlas of the human brain: theory and rationale for its development. the international consortium for brain mapping (ICBM)," *NeuroImage*, vol. 2, no. 2, pp. 89–101, 1995-06.

[32] R. S. Desikan, F. Ségonne, B. Fischl, B. T. Quinn, B. C. Dickerson, D. Blacker, R. L. Buckner, A. M. Dale, R. P. Maguire, B. T. Hyman, M. S. Albert, and R. J. Killiany, "An automated labeling system for subdividing the human cerebral cortex on MRI scans into gyral based regions of interest," *Neuroimage*, vol. 31, no. 3, pp. 968–980, 2006-07.

[33] M. C. Corsi, M. Chavez, D. Schwartz, N. George, L. Hugueville, A. E. Kahn, S. Dupont, D. S. Bassett, and F. De Vico Fallani, "Functional disconnection of associative cortical areas predicts performance during bci training," *NeuroImage*, vol. 209, p. 116500, 2020.

[34] D. Wales and J. P. K. Doye, "Global optimization by basin-hopping and the lowest energy structures of lennard-jones clusters containing up to 110 atoms," *Journal of Physical Chemistry A*, vol. 101, no. 28, pp. 5111–5116, 1997.

[35] P. Verma, S. Nagarajan, and A. Raj, "Stability and dynamics of a spectral graph model of brain oscillations," *Network Neuroscience*, pp. 1–43, 07 2022.

[36] B. Rosner, R. J. Glynn, and M.-L. T. Lee, "The wilcoxon signed rank test for paired comparisons of clustered data," *Biometrics*, vol. 62, no. 1, pp. 185–192, 2006.

[37] Y. Benjamini and D. Yekutieli, "The control of the false discovery rate in multiple testing under dependency," *The Annals of Statistics*, vol. 29, no. 4, pp. 1165–1188, 2001.

[38] M. Friedman, "A comparison of alternative tests of significance for the problem of *m* rankings," *The annals of mathematical statistics*, vol. 11, no. 1, pp. 86–92, 1940.

[39] J. C. Pinheiro and D. M. Bates, *Mixed-Effects Models in S and S-PLUS*. New York: Springer Science & Business Media, 2000.

[40] B. H. Jansen, G. Zouridakis, and M. E. Brandt, "A neurophysiologically-based mathematical model of flash visual evoked potentials," *Biological cybernetics*, vol. 68, pp. 275–283, 1993.

[41] B. H. Jansen and V. G. Rit, "Electroencephalogram and visual evoked potential generation in a mathematical model of coupled cortical columns," *Biological cybernetics*, vol. 73, no. 4, pp. 357–366, 1995.

[42] O. David and K. J. Friston, "A neural mass model for meg/eeg: coupling and neuronal dynamics," *NeuroImage*, vol. 20, no. 3, pp. 1743–1755, 2003.

[43] T. Donoghue, M. Haller, E. J. Peterson, P. Varma, P. Sebastian, R. Gao, T. Noto, A. H. Lara, J. D. Wallis, R. T. Knight, *et al.*, "Parameterizing neural power spectra into periodic and aperiodic components," *Nature neuroscience*, vol. 23, no. 12, pp. 1655–1665, 2020.

[44] E. Nozari, M. A. Bertolero, J. Stiso, L. Caciagli, E. J. Cornblath, X. He, A. S. Mahadevan, G. J. Pappas, and D. S. Bassett, "Macroscopic resting-state brain dynamics are best described by linear models," *Nature biomedical engineering*, vol. 8, no. 1, pp. 68–84, 2024.

[45] F. Wendling, F. Bartolomei, J. J. Bellanger, and P. Chauvel, "Epileptic fast activity can be explained by a model of impaired gabaergic dendritic inhibition," *The European Journal of Neuroscience*, vol. 15, no. 9, pp. 1499–1508, 2002.

[46] G. Pfurtscheller and F. H. Lopes da Silva, "Event-related eeg/meg synchronization and desynchronization: basic principles," *Clinical Neurophysiology*, vol. 110, no. 11, pp. 1842–1857, 1999.

[47] A. Destexhe, M. Rudolph, and D. Paré, "High-conductance state of neocortical neurons in vivo," *Nature Reviews Neuroscience*, vol. 4, no. 9, pp. 739–751, 2003.

[48] S. Rose, A. Guzzetta, K. Pannek, R. Boyd, M. Bastiani, L. Emsell, C. Falconer, S. Fiori, and D. K. Jones, "Structural hemispheric asymmetries in the human precentral gyrus hand representation," *Neuroscience*, vol. 210, pp. 211–221, 2012.

[49] J. Wang, Y. Yang, L. Fan, C. Xu, P. T. Fox, S. B. Eickhoff, C. Yu, and T. Jiang, "Correspondent functional topography of the human left inferior parietal lobule at rest and under task revealed using resting-state fmri and coactivation based parcellation," *Human Brain Mapping*, vol. 38, no. 3, pp. 1659–1675, 2017.

[50] D. Balslev, B. Odoj, and H.-O. Karnath, "Role of somatosensory cortex in visuospatial attention," *The Journal of Neuroscience*, vol. 33, no. 46, pp. 18311–18318, 2013.

[51] E. Kropf, S. K. Syan, L. Minuzzi, and B. N. Frey, "From anatomy to function: the role of the somatosensory cortex in emotional regulation," *Revista Brasileira de Psiquiatria*, vol. 41, no. 3, pp. 261–269, 2019.

[52] A. E. Cavanna and M. R. Trimble, "The precuneus: a review of its functional anatomy and behavioural correlates," *Brain*, vol. 129, no. Pt 3, pp. 564–583, 2006.

[53] R. J. Perry and S. Zeki, "The neurology of saccades and covert shifts in spatial attention: an event-related fmri study," *Brain: A Journal of Neurology*, vol. 123, no. Pt 11, pp. 2273–2288, 2000.

[54] E. Ben-Shabat, F. Matyas, G. S. Pell, A. Brodtmann, and L. M. Carey, "The right supramarginal gyrus is important for proprioception in healthy and stroke-affected participants: A functional mri study," *Frontiers in Neurology*, vol. 6, p. 248, 2015.

[55] B. N. Lundstrom, M. Ingvar, and K. M. Petersson, "Isolating the retrieval of imagined pictures during episodic memory: activation of the left precuneus and left prefrontal cortex," *NeuroImage*, vol. 20, no. 4, pp. 1934–1943, 2003.

[56] G. Plomp, A. Hervais-Adelman, L. Astolfi, and C. M. Michel, "Functional specialization and dynamic resource allocation in visual cortex," *Human Brain Mapping*, vol. 31, no. 1, pp. 1–13, 2010.

[57] A. Qureshy, R. Kawashima, M. B. Imran, M. Sugiura, R. Goto, K. Okada, K. Inoue, K. Horie, S. Yoshioka, and H. Fukuda, "Functional mapping of human brain in olfactory processing: a pet study," *Journal of Neurophysiology*, vol. 84, no. 3, pp. 1656–1666, 2000.

[58] E. T. Rolls, "The cingulate cortex and limbic systems for emotion, action, and memory," *Brain Structure and Function*, vol. 224, no. 9, pp. 3001–3018, 2019.

[59] R. Leech and D. J. Sharp, "The role of the posterior cingulate cortex in cognition and disease," *Brain*, vol. 137, no. Pt 1, pp. 12–32, 2014.

[60] Y. Lerner, T. Hendler, D. Ben-Bashat, M. Harel, and R. Malach, "Object-completion effects in the human lateral occipital complex," *Cerebral Cortex*, vol. 12, no. 2, pp. 163–177, 2002.

[61] Y. Kamitani and F. Tong, "Decoding seen and attended motion directions from activity in the human visual cortex," *Current Biology*, vol. 16, no. 11, pp. 1096–1102, 2006.

[62] T. D. Waberski, R. Gobbelé, K. Lamberty, H. Buchner, J. C. Marshall, and G. R. Fink, "Timing of visuo-spatial information processing: electrical source imaging related to line bisection judgements," *Neuropsychologia*, vol. 46, no. 5, pp. 1201–1210, 2008.

[63] A. M. Owen, B. Milner, M. Petrides, and A. C. Evans, "A specific role for the right parahippocampal gyrus in the retrieval of object-location: a positron emission tomography study," *Journal of Cognitive Neuroscience*, vol. 8, no. 6, pp. 588–602, 1996.

[64] V. D. Bohbot, M. Kalina, K. Stepankova, N. Spackova, M. Petrides, and L. Nadel, "Memory deficits characterized by patterns of lesions to the hippocampus and parahippocampal cortex," *Annals of the New York Academy of Sciences*, vol. 911, pp. 355–368, 2000.

[65] M. C. Thompson, "Critiquing the concept of BCI illiteracy," *Science and Engineering Ethics*, 2018-08-16.

[66] G. Huang *et al.*, "Discrepancy between inter- and intra-subject variability in eeg-based motor imagery brain-computer interface: Evidence from multiple perspectives," *Frontiers in Neuroscience*, vol. 17, p. 1122661, Feb 2023.

[67] S. Saha and M. Baumert, "Intra- and inter-subject variability in eeg-based sensorimotor brain computer interface: A review," *Frontiers in Computational Neuroscience*, vol. 13, p. 87, Jan 2020.

[68] S. D. McDougle, R. B. Ivry, and J. A. Taylor, "Taking Aim at the Cognitive Side of Learning in Sensorimotor Adaptation Tasks," *Trends Cogn. Sci. (Regul. Ed.)*, vol. 20, pp. 535–544, July 2016.

[69] S. Hétu, M. Grégoire, A. Saimpont, M.-P. Coll, F. Eugène, P.-E. Michon, and P. L. Jackson, "The neural network of motor imagery: an ALE meta-analysis," *Neuroscience and Biobehavioral Reviews*, vol. 37, pp. 930–949, June 2013.

[70] R. M. Hardwick, S. Caspers, S. B. Eickhoff, and S. P. Swinnen, "Neural correlates of action: Comparing meta-analyses of imagery, observation, and execution," *Neuroscience & Biobehavioral Reviews*, vol. 94, pp. 31–44, Nov. 2018.

[71] E. Dayan and L. G. Cohen, "Neuroplasticity subserving motor skill learning," *Neuron*, vol. 72, pp. 443–454, Nov. 2011.

[72] K. Ganguly and J. M. Carmena, "Emergence of a Stable Cortical Map for Neuroprosthetic Control," *PLOS Biology*, vol. 7, p. e1000153, July 2009.

[73] C. T. Moritz, S. I. Perlmutter, and E. E. Fetz, "Direct control of paralysed muscles by cortical neurons," *Nature*, vol. 456, pp. 639–642, Dec. 2008.

[74] J. M. Carmena, M. A. Lebedev, R. E. Crist, J. E. O'Doherty, D. M. Santucci, D. F. Dimitrov, P. G. Patil, C. S. Henriquez, and M. A. L. Nicolelis, "Learning to Control a Brain–Machine Interface for Reaching and Grasping by Primates," *PLOS Biology*, vol. 1, p. e42, Oct. 2003.

[75] A. Orsborn, H. Moorman, S. Overduin, M. Shanechi, D. Dimitrov, and J. Carmena, "Closed-Loop Decoder Adaptation Shapes Neural Plasticity for Skillful Neuroprosthetic Control," *Neuron*, vol. 82, pp. 1380–1393, June 2014.

[76] A. L. Orsborn and B. Pesaran, "Parsing learning in networks using brain-machine interfaces," *Current Opinion in Neurobiology*, vol. 46, pp. 76–83, 2017.

[77] M. C. Dadarlat, R. A. Canfield, and A. L. Orsborn, "Neural Plasticity in Sensorimotor Brain–Machine Interfaces," *Annual Review of Biomedical Engineering*, vol. 25, pp. 51–76, June 2023. Publisher: Annual Reviews.

[78] F. Pichiorri, G. Morone, M. Petti, J. Toppi, I. Pisotta, M. Molinari, S. Paolucci, M. Inghilleri, L. Astolfi, F. Cincotti, and D. Mattia, "Brain–computer interface boosts motor imagery practice during stroke recovery," *Annals of Neurology*, vol. 77, 2015.

[79] J. D. Wander, T. Blakely, K. J. Miller, K. E. Weaver, L. A. Johnson, J. D. Olson, E. E. Fetz, R. P. N. Rao, and J. G. Ojemann, "Distributed cortical adaptation during learning of a brain–computer interface task," *Proceedings of the National Academy of Sciences of the United States of America*, vol. 110, pp. 10818–10823, June 2013.

[80] S. Perdikis, L. Tonin, S. Saeedi, C. Schneider, and J. d. R. Millán, "The Cybathlon BCI race: Successful longitudinal mutual learning with two tetraplegic users," *PLoS Biology*, vol. 16, May 2018.

[81] A. Bamdadian, C. Guan, K. K. Ang, and J. Xu, "The predictive role of pre-cue EEG rhythms on MI-based BCI classification performance," *Journal of Neuroscience Methods*, vol. 235, pp. 138–144, Sept. 2014.

[82] M. Grosse-Wentrup and B. Schölkopf, "High -power predicts performance in sensorimotor-rhythm brain-computer interfaces," *J Neural Eng*, vol. 9, p. 046001, Aug. 2012.

[83] C. Jeunet, B. N'Kaoua, S. Subramanian, M. Hachet, and F. Lotte, "Predicting Mental Imagery-Based BCI Performance from Personality, Cognitive Profile and Neurophysiological Patterns," *PLoS ONE*, vol. 10, no. 12, p. e0143962, 2015.

[84] M. Husain and P. Nachev, “Space and the parietal cortex,” *Trends in Cognitive Sciences*, vol. 11, no. 1, pp. 30–36, 2007.

[85] M. Koenigs, A. K. Barbey, B. R. Postle, and J. Grafman, “Superior parietal cortex is critical for the manipulation of information in working memory,” *The Journal of Neuroscience*, vol. 29, no. 47, pp. 14980–14986, 2009.

[86] N. Insel, D. M. Barch, S. Walther, F. Krueger, J. A. Waltz, J. D. Cohen, and J. M. Gold, “Irrelevance by inhibition: Learning, computation, and implications for schizophrenia,” *PLoS Computational Biology*, vol. 14, p. e1006315, Aug 2018.

[87] D. Borsook, R. Veggeberg, N. Erpelding, R. Borra, C. Linnman, R. Burstein, and L. Becerra, “The insula: A "hub of activity" in migraine,” *The Neuroscientist*, vol. 22, no. 6, pp. 632–652, 2016.

[88] Y. Takenaka, T. Suzuki, and K. Sugawara, “Time course effect of corticospinal excitability for motor imagery,” *European Journal of Neuroscience*, vol. 54, pp. 6123 – 6134, 2021.

[89] T. A. Yousry, U. D. Schmid, H. Alkadhi, D. Schmidt, A. Peraud, A. Buettner, and P. Winkler, “Localization of the motor hand area to a knob on the precentral gyrus. a new landmark,” *Brain: A Journal of Neurology*, vol. 120, no. Pt 1, pp. 141–157, 1997.

[90] C. A. Porro, V. Cettolo, M. P. Francescato, and P. Baraldi, “Ipsilateral involvement of primary motor cortex during motor imagery,” *The European Journal of Neuroscience*, vol. 12, no. 8, pp. 3059–3063, 2000.

[91] A. D. Garcia and E. A. Buffalo, “Anatomy and function of the primate entorhinal cortex,” *Annual Review of Vision Science*, vol. 6, pp. 411–432, 2020.

[92] T. Venot, A. Desbois, M. C. Corsi, L. Hugueville, L. Saint-Bauzel, and F. De Vico Fallani, “Intentional binding for noninvasive BCI control,” *Journal of Neural Engineering*, vol. 21, no. 4, 2024-07-25.

[93] B. Fischl, M. I. Sereno, R. B. Tootell, and A. M. Dale, “High-resolution intersubject averaging and a coordinate system for the cortical surface,” *Human Brain Mapping*, vol. 8, no. 4, pp. 272–284, 1999.

[94] J. DiGuiseppi and P. Tadi, “Neuroanatomy, postcentral gyrus,” in *StatPearls*, StatPearls Publishing, 2025.

[95] K. Zilles and N. Palomero-Gallagher, “4.14 - the architecture of somatosensory cortex,” in *The Senses: A Comprehensive Reference (Second Edition)* (B. Fritzsch, ed.), pp. 225–260, Elsevier, 2020.

[96] T. Venot, *Design and evaluation of a multimodal control of a robotic arm with a Brain Computer Interface*. These de doctorat, Sorbonne université, Nov. 2023.

[97] R. M. El-Baba and M. P. Schury, “Neuroanatomy, frontal cortex,” in *StatPearls*, StatPearls Publishing, 2025.

[98] Y. Munakata, S. A. Herd, C. H. Chatham, B. E. Depue, M. T. Banich, and R. C. O’Reilly, “A unified framework for inhibitory control,” *Trends in Cognitive Sciences*, vol. 15, no. 10, pp. 453–459, 2011.

[99] K. Konstantopoulos and D. Giakoumettis, “Chapter 1 - basic knowledge on neuroanatomy and neurophysiology of the central nervous system,” in *Neuroimaging in Neurogenic Communication Disorders* (K. Konstantopoulos and D. Giakoumettis, eds.), pp. 1–30, Academic Press, 2023.

[100] F. Binkofski and G. Buccino, "Chapter 24 - the role of the parietal cortex in sensorimotor transformations and action coding," in *Handbook of Clinical Neurology* (G. Vallar and H. B. Coslett, eds.), vol. 151 of *The Parietal Lobe*, pp. 467–479, Elsevier, 2018-01-01.

[101] J. Henderson, W. Choi, and S. Luke, "Morphology of primary visual cortex predicts individual differences in fixation duration during text reading," *Journal of Cognitive Neuroscience*, vol. 26, pp. 2880–2888, 2014.

[102] E. T. Rolls, W. Cheng, and J. Feng, "The orbitofrontal cortex: reward, emotion and depression," *Brain Communications*, vol. 2, no. 2, p. fcaa196, 2020-11-16.

[103] J. D. Wallis and M. F. S. Rushworth, "Chapter 22 - integrating benefits and costs in decision making," in *Neuroeconomics (Second Edition)* (P. W. Glimcher and E. Fehr, eds.), pp. 411–433, Academic Press, 2014-01-01.

[104] A. Puce and M. S. Hämäläinen, "A Review of Issues Related to Data Acquisition and Analysis in EEG/MEG Studies," *Brain Sci*, vol. 7, May 2017.

[105] S. P. Ahlfors, J. Han, J. W. Belliveau, and M. S. Hämäläinen, "Sensitivity of MEG and EEG to Source Orientation," *Brain Topography*, vol. 23, pp. 227–232, Sept. 2010.

Supplementary Document

1 Materials & Methods

1.1 Model Description

The linearized NMM (17; 18; 19) used to extract excitatory and inhibitory neuronal subpopulation parameters. The model at the mesoscopic level (regional model), for every region k (k varies from 1 to N and N is the total number of regions) based on the DK parcellation, is modeled as the sum of excitatory signals $x_{\mathrm{e}}(t)$ and inhibitory signals $x_{\mathrm{i}}(t)$. Both excitatory and inhibitory signal dynamics consist of a decay of the individual signals with a fixed neural gain, incoming signals from populations that couple the excitatory and inhibitory signals, and input Gaussian white noise for resting state and colored noise for mentally active state. The model equations for the excitatory and inhibitory signals for every region of the DK atlas that describes the rate of change of signal or firing rate in excitatory and inhibitory neural sub-populations are:

$$\frac{\mathrm{d}x_{\mathrm{e}}(t)}{\mathrm{d}t} = -f_{\mathrm{e}}(t) \star \frac{1}{\tau_{\mathrm{e}}}\big(g_{\mathrm{ee}}x_{\mathrm{e}}(t) - g_{\mathrm{ei}}f_{\mathrm{i}}(t) \star x_{\mathrm{i}}(t)\big) + p(t)\ , \text{ and} \tag{7}$$

$$\frac{\mathrm{d}x_{\mathrm{i}}(t)}{\mathrm{d}t} = -f_{\mathrm{i}}(t) \star \frac{1}{\tau_{\mathrm{i}}}\big(g_{\mathrm{ii}}x_{\mathrm{i}}(t) + g_{\mathrm{ei}}f_{\mathrm{e}}(t) \star x_{\mathrm{e}}(t)\big) + p(t)\ . \tag{8}$$

The symbols used in the equations are as follows: $\star$ denotes convolution; parameters g_{ee}, g_{ii}, and g_{ei} represent neural gains for excitatory, inhibitory and for coupling neural gain between excitatory and inhibitory populations, respectively; τ_{e} and τ_{i} are the time scales of excitatory and inhibitory populations, respectively; $p(t)$ is extrinsic presynaptic input/stimulus; $f_{\mathrm{e}}(t)$ and $f_{\mathrm{i}}(t)$ are average neural impulse response functions. Note that the asymetry in the two equations is to indicate that excitatory signals enhance inhibitory signals while inhibitory signals suppress excitatory signals, and therefore the two differential equations are not

identical to each other. In this way, they are describing the activity of the excitatory and inhibitory neuronal populations and how they interact with each other. Therefore, the differential equations have a biophysical interpretation.

Parameters g_{ei}, g_{ii}, τ_{e}, and τ_{i} were estimated for each region of interest (ROI), while g_{ee} was fixed at 1 for parameter identifiability. For parameter identifiability, any one of the gain parameters need to be fixed. Based on model stability analysis by investigating how the poles of the transfer function shift depending on the model parameters, we observed that the model is stable for a very narrow range of g_{ee} around 1. Therefore, we decided to fix g_{ee} to be 1.

We can get a closed-form solution in the Fourier domain since the two equations above are linear, as shown below. The Fourier transform $F()$ is taken at an angular frequency ω, which is equal to $2\pi f$, where f is the frequency in Hz. The Fourier transform of equations 7 and 8 will be the following, where $F(x_{\mathrm{e}}(t)) = X_{\mathrm{e}}(\omega)$ and $F(x_{\mathrm{i}}(t)) = X_{\mathrm{i}}(\omega)$, and j is the imaginary unit.

$$\mathrm{j}\omega X_{\mathrm{e}}(\omega) = -\frac{F_{\mathrm{e}}(\omega)}{\tau_{\mathrm{e}}}(g_{\mathrm{ee}}X_{\mathrm{e}}(\omega) - g_{\mathrm{ei}}F_{\mathrm{i}}(\omega)X_{\mathrm{i}}(\omega)) + P(\omega)\ , \text{ and} \tag{9}$$

$$\mathrm{j}\omega X_{\mathrm{i}}(\omega) = -\frac{F_{\mathrm{i}}(\omega)}{\tau_{\mathrm{i}}}(g_{\mathrm{ii}}X_{\mathrm{i}}(\omega) + g_{\mathrm{ei}}F_{\mathrm{e}}(\omega)X_{\mathrm{e}}(\omega)) + P(\omega)\ . \tag{10}$$

On solving the above equations 9 and 10, $X_{\mathrm{e}}(\omega)$ and $X_{\mathrm{i}}(\omega)$ are:

$$X_{\mathrm{e}}(\omega) = \frac{1 + \frac{F_1}{\tau_{\mathrm{e}}F_2}}{F_3 + \frac{F_1^2}{\tau_{\mathrm{e}}\tau_{\mathrm{i}}F_2}}P(\omega)\ , \text{ and}$$

$$X_{\mathrm{i}}(\omega) = \frac{1 - \frac{F_1}{\tau_{\mathrm{i}}F_3}}{F_2 + \frac{F_1^2}{\tau_{\mathrm{e}}\tau_{\mathrm{i}}F_3}}P(\omega)\ ,$$

where

$$F_1 = g_{\mathrm{ei}}F_{\mathrm{e}}(\omega)F_{\mathrm{i}}(\omega), \quad F_2 = \mathrm{j}\omega + \frac{g_{\mathrm{ii}}}{\tau_{\mathrm{i}}}F_{\mathrm{i}}(\omega), \quad \text{and} \quad F_3 = \mathrm{j}\omega + \frac{g_{\mathrm{ee}}}{\tau_{\mathrm{e}}}F_{\mathrm{e}}(\omega).$$

Then, the transfer functions $H_{\mathrm{e}}(\omega)$ and $H_{\mathrm{i}}(\omega)$ can be separated, and we get:

$$X_{\mathrm{e}}(\omega) = H_{\mathrm{e}}(\omega)P(\omega), \quad \text{and} \quad X_{\mathrm{i}}(\omega) = H_{\mathrm{i}}(\omega)P(\omega).$$

Thus, for the total neural population at each region:

$$X_{\mathrm{local}}(\omega) = (H_{\mathrm{e}}(\omega) + H_{\mathrm{i}}(\omega))P(\omega) \tag{11}$$

The extrinsic input $p(t)$ is characterized by its power spectral density (PSD) $S_p(\omega)$, which is assumed to be identical for excitatory and inhibitory local populations within each region. To simulate RS condition, $p(t)$ was modeled as white noise, characterized by a constant PSD. To simulate the MI condition, $p(t)$ was modeled as a colored noise with a power-law spectrum, such that $S_p(\omega) \propto 1/f^k$, where $k \in [0, 1]$.

Given the linear time-invariant nature of the model, the simulated output power spectral density was obtained as:

$$S_{X_{\mathrm{local}}}(\omega) = \mathbb{E}[|X_{\mathrm{local}}(\omega)|^2] \propto |(H_{\mathrm{e}}(\omega) + H_{\mathrm{i}}(\omega))|^2 S_p(\omega) \tag{12}$$

where $\mathbb{E}[\cdot]$ denotes expectation. The resulting spectra were expressed in dB scale as $10 \log_{10} S_{X_{\text{local}}}(\omega)$. Although the equations include a stochastic input term, we do not solve them in the time domain as stochastic differential equations. Our analysis is restricted to second-order statistics of the system output, which can be obtained directly in the frequency domain under assumptions of linearity and stationarity. Hence, the spectral properties of $p(t)$ are defined in-terms of PSD, obtained from second-order frequency domain statistics as $S_p(\omega) \propto \mathbb{E}[|P(\omega)|^2]$, where $P(\omega)$ is Fourier transform of finite-length realization of the input process. Accordingly, our analysis focuses exclusively on PSDs, which are deterministic quantities characterizing the second-order structure of the stochastic signals.

2 Results

Replication with EEG We replicated the condition effect analysis with EEG modeled data (refer to Fig. S6 and Table S2). No training effect has been observed (Friedman test, $p > 0.05$). Most of the significant conditions effects were observed from session 4. For g_{ei}, such effects are involved in particular motor areas (left *precentral gyrus*), parietal lobe (left *inferior parietal* lobule) and occipital areas (bilateral *cuneus*). Similarly, for g_{ii}, the bilateral cuneus showed significant effects. Lastly, for τ_{e}, the right supramarginal gyrus was significantly affected. These findings suggest session-specific variations in brain activity between MI and RS, mainly with session 4 that showed the most pronounced differences. Similarly to MEG, condition effects observed with g_{ei} and g_{ii} were associated with lower values in RS compared to MI, whereas τ_{e} exhibited lower values in MI than in RS.

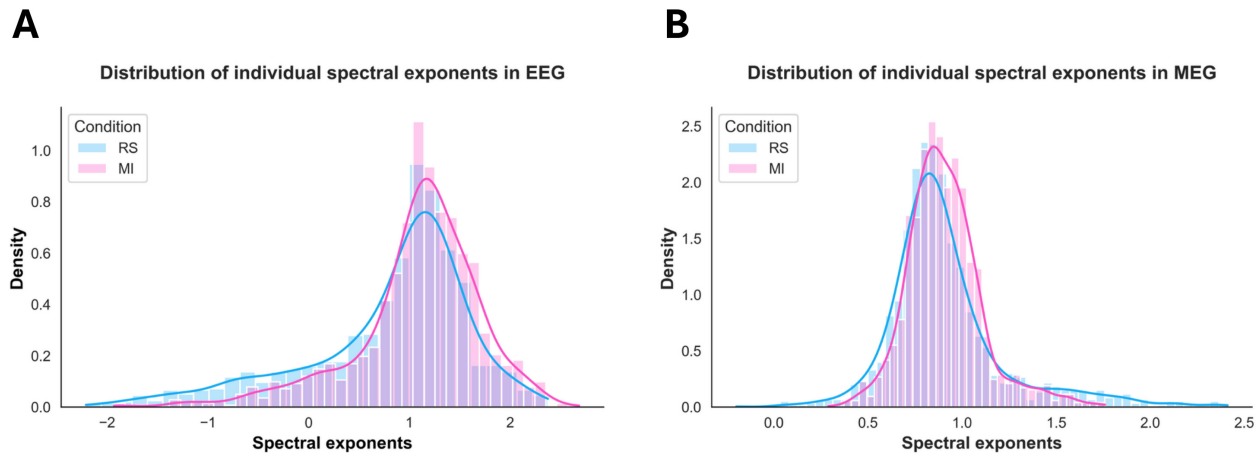

Figure S1: **Distribution of spectral exponents in rest (RS) and motor-imagery (MI) condition:** A, B exhibit histogram distribution of individual spectral exponents in RS and MI, with exponents in both conditions nearly completely overlapping in both EEG and MEG, respectively.

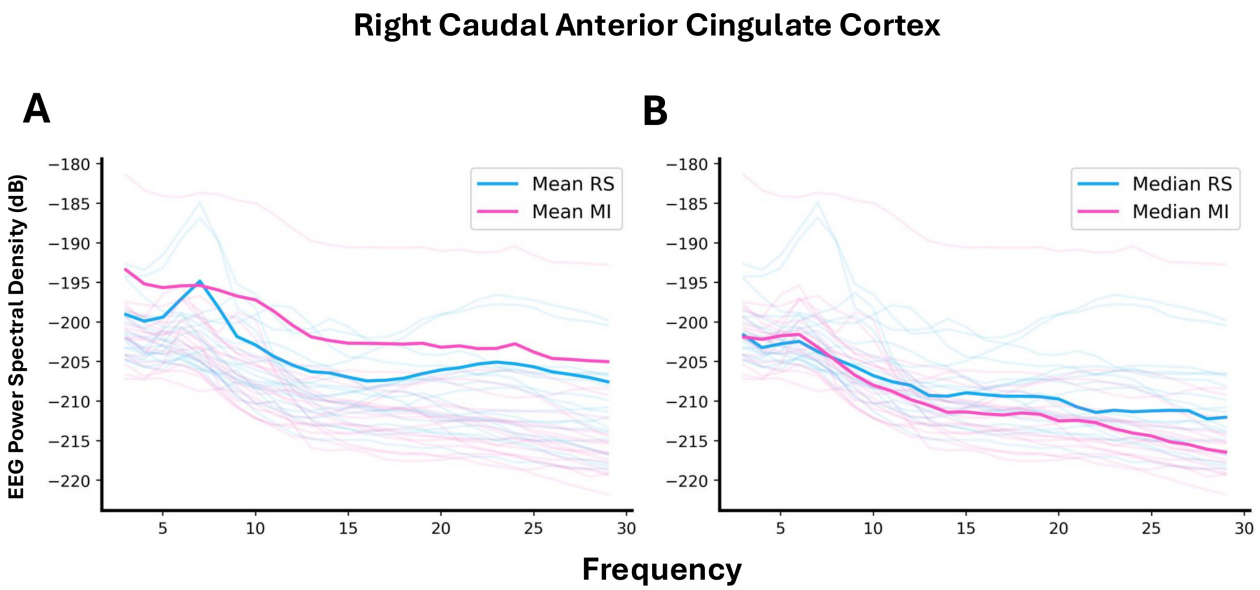

Figure S2: **Mean Vs. Median spectra:** Example comparison of median versus mean of spectra for the Right Caudal Anterior Cingulate region. Median spectra in B provides better representation of 19 individual spectra than mean spectra in A in both rest (RS) and motor-imagery (MI) condition, as few individual spectra skew the overall representation in case of mean.

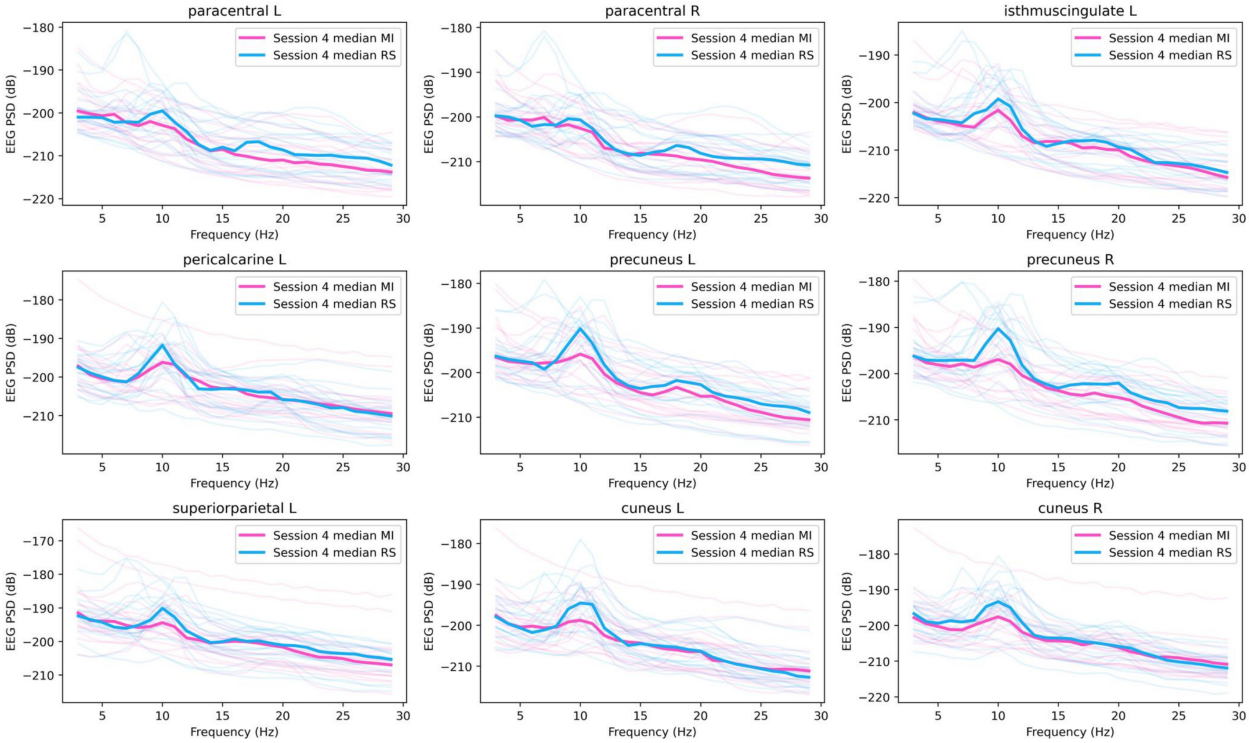

Figure S3: Representation of changes in power spectral density (PSD) in session 4 EEG along the frequency range (3-30 Hz) in a select few regions.

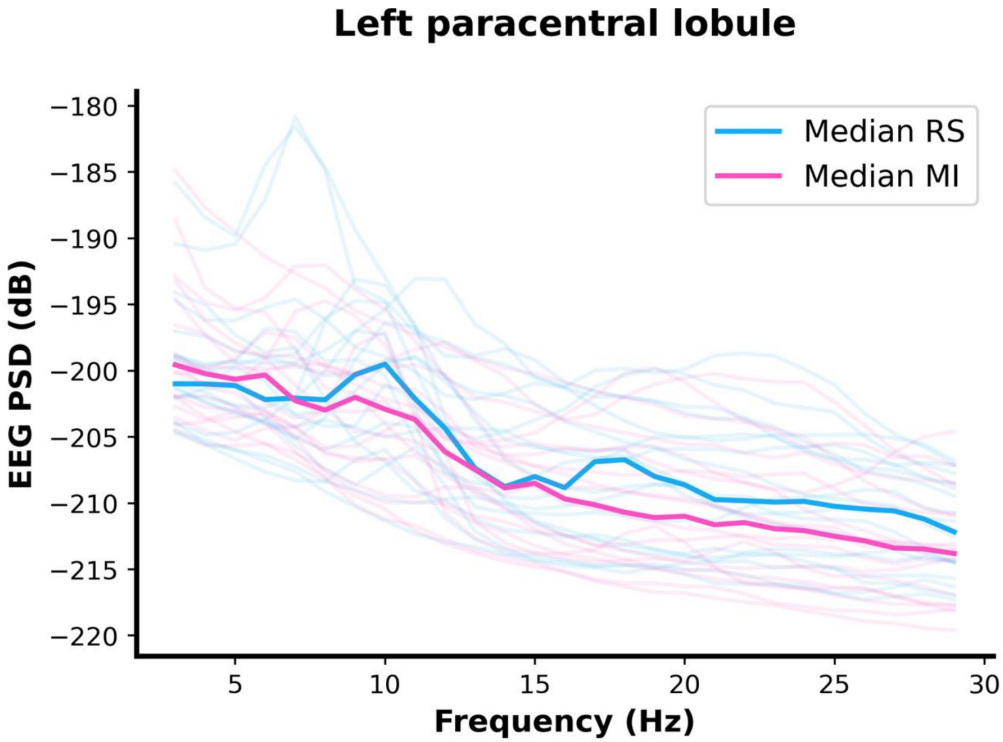

Figure S4: **Changes in EEG – Power Spectral Density (PSD) in Left paracentral lobule:** It shows that the changes in PSD in case of rest (RS) and motor-imagery (MI) condition, with median of the distribution of 19 spectra in both the conditions in bold. The alpha and beta peak can be observed in both the conditions.

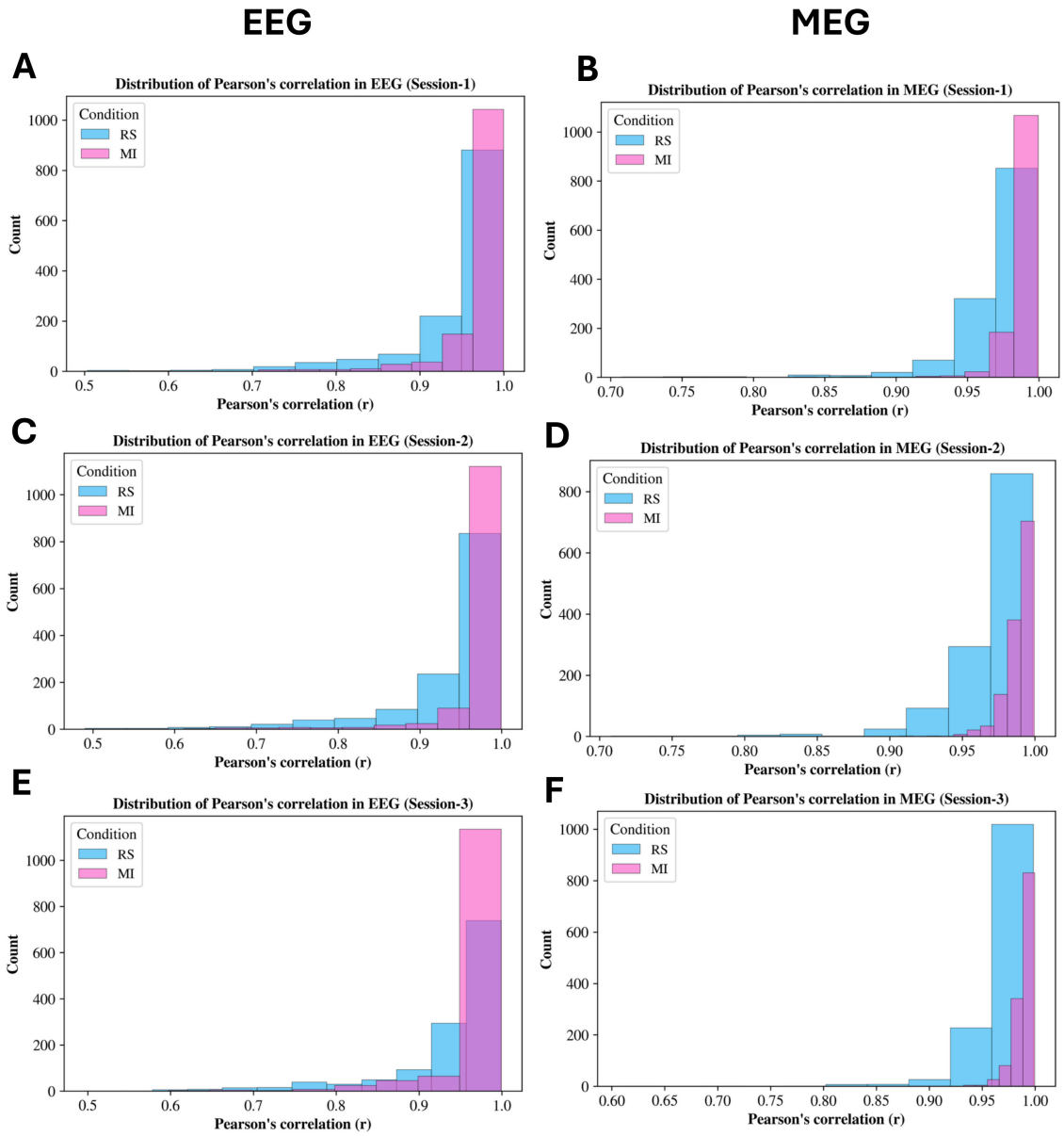

Figure S5: **Pearson correlation coefficient between modeled and actual PSD in both rest (RS) and motor-imagery (MI)**: A, B: Distribution of the coefficient is more than 0.90 in most cases in both RS and MI condition in session 1 EEG and MEG, respectively; C,D: Similar to the above fig, here it shows in session 2 EEG, MEG respectively; E, F: it Shows the distribution in session 3 EEG, MEG respectively

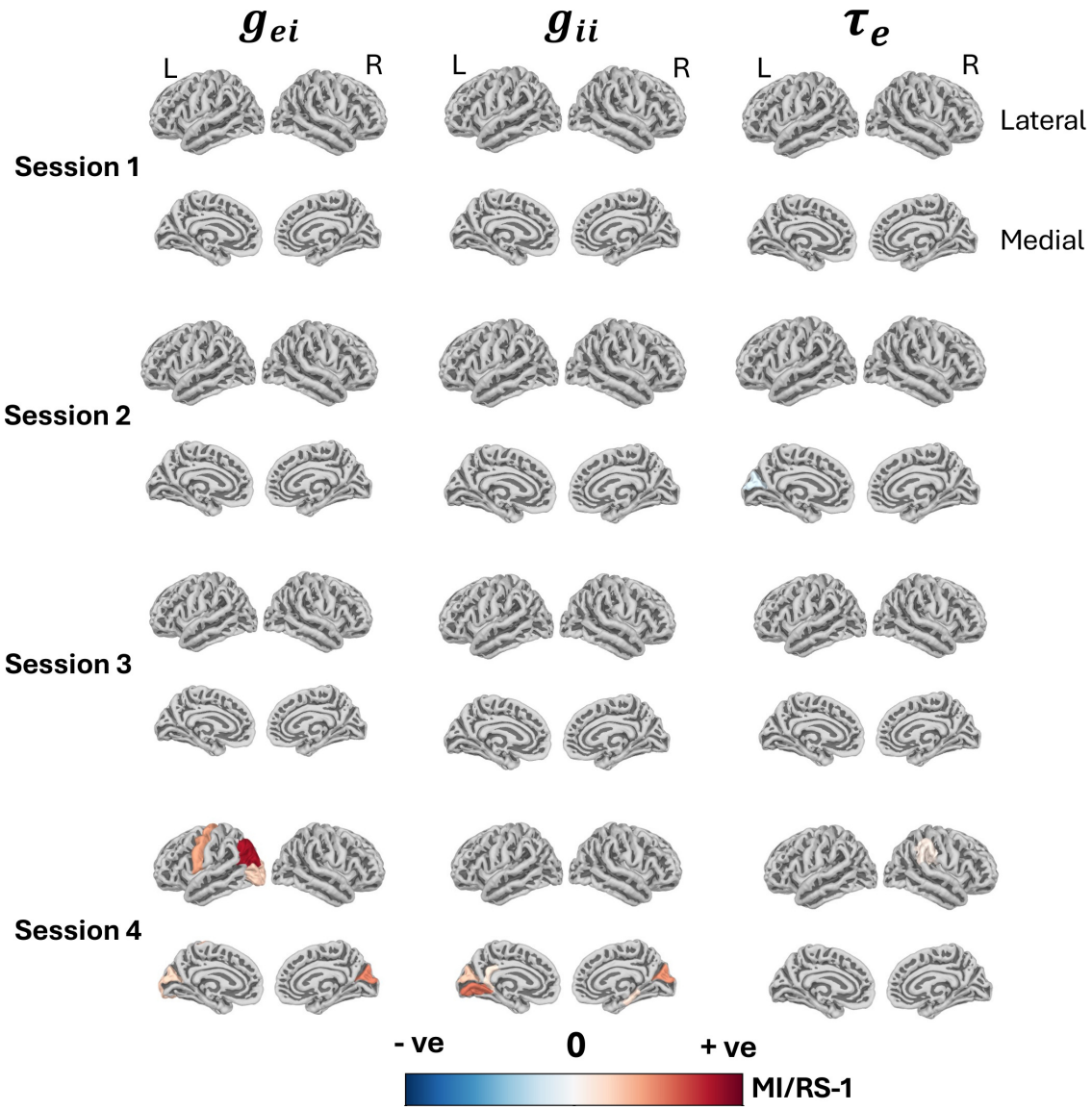

Figure S6: **EEG – based condition effect analysis in BCI learning:** The highlighted colored regions show statistically significant ($p_{\text{FDR}} < 0.05$) condition effect for MI Vs RS for the three EEG fitted model parameters (g_{ei}, g_{ii}, τ_{e}) respectively in every session. This shows functional reorganization across sessions as various cortical regions are getting activated for the MI BCI task in the 19 subjects' group. Minimum and maximum range of mean (MI/RS-1) for the parameters across sessions are (-0.38, +184.74), (-0.418, +374.87), (-0.365, +1.449) for g_{ei}, g_{ii}, τ_{e} respectively.

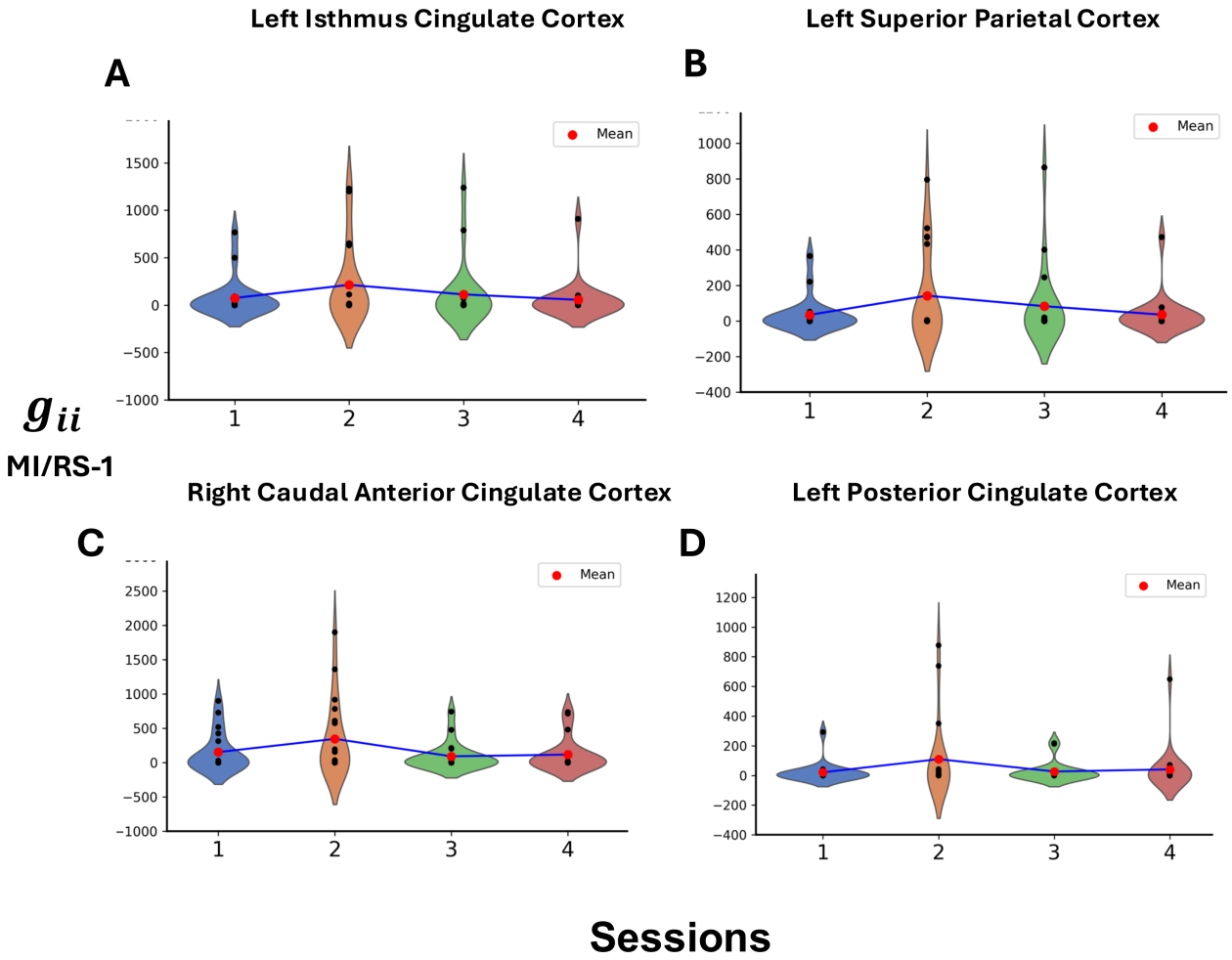

Figure S7: **Changes in relative values ($\frac{\mathbf{MI}}{\mathbf{RS}}$-1) of g_{ii} over time in EEG– session after session:**
The left isthmus cingulate (A), superior parietal (B), posterior cingulate (D) and Right caudal anterior cingulate cortex (C)–In each of these regions we see there is a change in the mean value of the distribution of 19 relative g_{ii} values over time, suggesting the effects of training sessions in these regions for BCI learning.

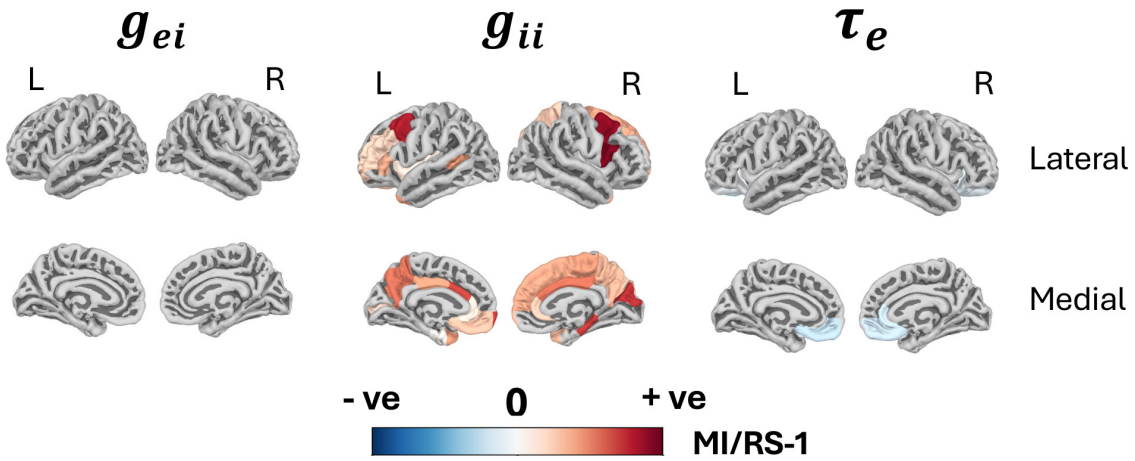

Figure S8: **Condition effect analysis for the independent dataset:**The highlighted colored regions show statistically significant ($p_{\text{FDR}} < 0.05$) condition effect between MI and RS for the three EEG fitted model parameters (g_{ei}, g_{ii}, τ_{e}) respectively. This show how various cortical regions are getting activated for MI BCI task. Minimum and maximum range of mean (MI/RS-1) for the parameters across sessions are (-0.287, +81.57), (-9.275, +416.3), (-0.36, +1.448) for (g_{ei}, g_{ii}, τ_{e}) respectively.

Table S1: Significant ROIs ($p_{\text{FDR}} < 0.05$) across MEG sessions, grouped by lobe

Session	g_{ei}	g_{ii}	τ_{e}
Session 1	Parietal (Right inferior and superior Parietal), Occipital (Left lateral Occipital), Frontal (Left pars Opercularis)	Temporal (Left transverse Temporal)	Temporal (Left banks of superior temporal sulcus (STS), Left Fusiform, Left inferior and middle Temporal, Left pars Opercularis, Left and right transverse Temporal), Occipital (Left and right Cuneus, Left and right Pericalcarine), Frontal (Left and right caudal middle Frontal, Left and right Precentral, Right superior Frontal), Parietal (Left Paracentral, Left and right Postcentral, Right Precuneus, Left and right Supramarginal), Limbic (Right Entorhinal, Right posterior Cingulate)
Session 2	Nil	Temporal (Left transverse Temporal)	Occipital (Left and right Cuneus, Left and right Pericalcarine), Temporal (Left Fusiform, Left Insula, Left pars Opercularis, Right pars Triangularis, Left transverse Temporal, Right transverse Temporal), Frontal (Right medial Orbitofrontal, Right Precentral), Parietal (Left Paracentral, Right Postcentral, Right Precuneus, Left superior Parietal, Right Supramarginal), Limbic (Left posterior Cingulate, Left rostral anterior Cingulate)
Session 3	Nil	Parietal (Left inferior parietal, Left lateral Occipital), Frontal (Left rostral middle frontal), Temporal (Left and right transverse temporal), Limbic (Right posterior Cingulate)	Temporal (Left banks STS, Left Inferior temporal, Left pars Opercularis, Left and right transverse temporal), Occipital (Left and right Cuneus, Left pericalcarine), Frontal (Right caudal middle Frontal, Left and right Precentral, Left superior Frontal), Parietal (Left inferior Parietal, Left and right Postcentral, Left and right superior Parietal, Right superior temporal, Left and right Supramarginal), Limbic (Right posterior Cingulate)
Session 4	Nil	Parietal (Right postcentral), Temporal (Left transverse temporal)	Temporal (Left banks STS, Left transverse temporal), Occipital (Left cuneus, Left pericalcarine), Frontal (Right precentral), Parietal (Left and right inferior parietal, Left and right paracentral, Left and right postcentral, Left and right supramarginal), Limbic (Left entorhinal, Right isthmus cingulate, Left and right posterior cingulate, Left and right precuneus)

Table S2: Significant ROIs ($p_{\text{FDR}} < 0.05$) across EEG sessions

Session	g_{ei}	g_{ii}	τ_{e}
Session 1	Nil	Nil	Nil
Session 2	Nil	Nil	Left Cuneus
Session 3	Nil	Nil	Nil
Session 4	Left and right Cuneus, Left inferior Parietal, Left lateral Occipital, Left Precentral	Left and right Cuneus, Left isthmus Cingulate, Left Lingual, Right Parahippocampal	Right Supramarginal